ROYAL SOCIETY OF CHEMISTRY

REVIEW ARTICLE

Evaluation of zinc sulfide heterostructures as catalysts for the transformation of CO_2 into valuable chemicals and clean energy generation

Onome Ejeromedoghene, [iD] *[a] Khadijat Olabisi Abdulwahab,[b] Inemesit Asukwo Udofia,[b] Moses Kumi[c] and Ayorinde Olufunke Nejo[b]

There are significant concerns about global warming and the energy crisis due to the rise in atmospheric carbon dioxide (CO_2) concentration and the depletion of fossil fuels. Converting CO_2 into organic molecules using the abundant solar energy would be a quick fix that would address both issues. Excess CO_2 is a major contributor to the greenhouse effect, which leads to global warming, extreme weather patterns, and a host of other environmental challenges. To tackle these problems, scientists are exploring novel approaches to adsorb CO_2, transform it into useful products, and then release it back into the atmosphere. Semiconductor materials play a crucial role in CO_2 reduction. Among these materials, zinc sulfide (ZnS) and doped ZnS have gained significant attention for the potential catalytic transformation of CO_2 into useful compounds. The semiconductor properties of ZnS and its derivatives make them particularly well-suited for this purpose. The present review provides a summary of the recent progress in the development of strategies for fabricating ZnS-based heterostructures with functional properties for CO_2 reduction. The mechanism of CO_2 conversion was also addressed with new insights into computational modelling. Lastly, future outlook on the development of catalytic ZnS-based materials for CO_2 reduction is provided.

1. Introduction

The release of CO_2 into the environment from different industrial plants and vehicular emissions has been responsible for serious environmental degradation problems like ozone layer depletion, climate change, ocean acidification, and global warming due to the burning and consumption of fossil-based fuels and chemical compounds over the years.[1] Driven by the incessant global energy crisis and environmental pollution concerns, several efforts have been channeled into tackling these issues by converting CO_2 into renewable energy sources (fuels) and value-added chemicals *via* hydrogenation and reforming to obtain CH_4, CO, formic acid, olefins and CH_3OH (Fig. 1) as promising alternatives to reduce the dependence on fossil fuels/chemicals.[2–5] In the transformation reaction, CO_2
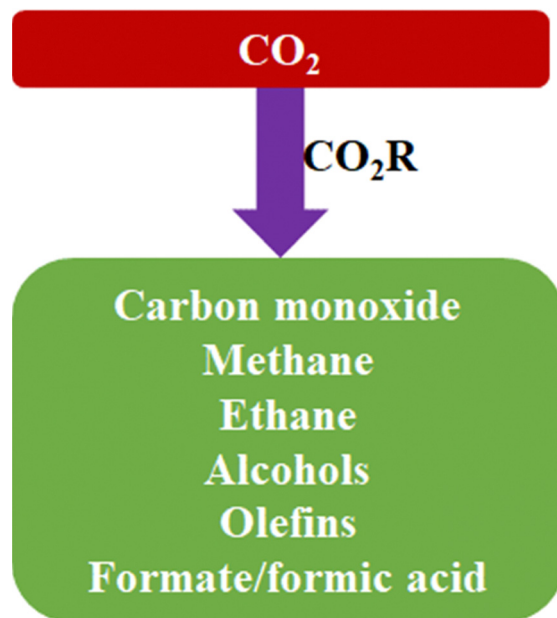
[a] *College of Chemistry, Chemical Engineering and Materials Science, Soochow University, 215123 Suzhou, Jiangsu Province, P. R. China.
E-mail: oejeromedoghene@suda.edu.cn*

[b] *Department of Chemistry, Faculty of Science, University of Lagos, Akoka, 101017, Yaba, Lagos, Nigeria*

[c] *Frontiers Science Center for Flexible Electronics (FSCFE), Xi'an Institute of Flexible Electronics (IFE), Xi'an Institute of Biomedical Materials and Engineering (IBME), Northwestern Polytechnical University (NPU), 127 West Youyi Road, Xi'an, Shaanxi 710072, P. R. China*

Fig. 1 Renewable energy and chemical compounds obtainable from CO_2 transformation.

can also produce hydrocarbons such as ethane/propane by dehydrogenation.[6] In principle, the dangers arising from CO_2 emissions are mainly attributed to the global energy imbalance and the balance can be restored or maintained by consciously reducing and stabilizing CO_2 emissions through agricultural practices, afforestation, and other advanced technologies.[7,8]

Amongst the advanced technologies for CO_2 conversion/transformation, the utilization of semiconducting transition metal oxides (TMOs), such as TiO_2, ZnO, ZrO_2, Al_2O_3, etc., has been extensively explored; unfortunately, the occupied O 2p orbital in the valence band results in a wider bandgap in metal oxides, which causes fast electron–hole recombination or sluggish hole transfer, and hence TMO utilization remains unsatisfactory for catalytic reactions.[9–11] In addition, the large effective mass of holes in metal oxides is also unfavorable for charge separation and transfer.[12]

Interestingly, transition metal sulfides (TMSs) are inexpensive earth-abundant elements with low toxicity and typically ZnS is the most studied TMS semiconductor that has received great attention for the reduction, conversion or transformation of CO_2. ZnS-based materials are characterized by their good photo-redox stability for the photocatalytic, electrochemical and photothermal reduction and transformation of CO_2 to value-added chemical products.[13]

Although ZnS has a fairly high theoretical photo-exciton generation efficiency with a large bandgap (≈ 3.7 eV) and fast recombination of charge carriers, which could limit the catalytic performance of ZnS in certain applications,[14,15] studies have established that doping the metal ion with dopants, such as carbon nitride, metal nanoparticles, graphene, etc.,[16–18] and generation of sulfur vacancies suppress the charge recombination and narrow down the bandgap of ZnS.[19] This has led to development of new hierarchical heterostructures with improved catalytic functions for the fast and high yield conversion of CO_2.[20,21] Noteworthily, the valence bands of ZnS-based semiconductors are primarily composed of the S 3p orbital, which has a lower potential energy than the O 2p orbital, and therefore, the sulfide-based semiconductors have narrower bandgaps and suitable redox potentials compared to the oxide-based semiconducting catalytic materials.[22]

This class of compounds also have specific advantages of promoting the kinetics of photoinduced charges, suitable electronic structures, adjustable optical properties, convenient electronic conductivity, prominent catalytic conversion performance and satisfactory potential of the conduction band minimum, which satisfies the required reduction potential for various CO_2 reduction reactions.[23,24] Although there are a wide range of reviews on TMOs and TMSs in the literature, the in-depth overview critically surveying the performance of ZnS and doped ZnS nanostructures and hierarchical heterostructures for CO_2 transformation and conversion is lacking. In this review, an up-to-date analysis of the recent progress in the development of strategies for fabricating ZnS-based heterostructures with functional properties was performed. Moreover, specific information on the electrocatalytic, photocatalytic, and photothermal catalytic properties of ZnS-based

heterostructures was provided. Particularly, the mechanistic pathways showing the transformation of CO_2 to value-added products and new insights into computational models for CO_2 conversion/transformation were provided. Finally, perspectives on future development prospects of ZnS-based materials for CO_2 reduction catalysis are put forward as an eye-opener towards designing effective and highly active catalytic systems for structure-related CO_2 reduction.

2. Fabrication strategies for ZnS- and doped ZnS-based heterostructures

ZnS heterostructures have been synthesized in different ways. Notably, these compounds have been extensively studied and combined with other materials to form nanocomposites, heterostructures or heterojunctions with superior chemical stability and strong visible absorption making them suitable catalysts for the reduction of CO_2. Doped ZnS has also been reported for the reduction of CO_2. Doping is a means of tuning the electronic structure, which involves introducing an additional energy level with the band gap to alter the energy band gap. This in turn affects the light absorption of the resulting doped material. ZnS has been doped with metals, non-metals and metalloids such as Cd, Zn, Ni, Cu, C and N. Fig. 2 summarizes the different methods that have been used for fabrication of ZnS and its heterostructures for CO_2 reduction.

2.1 Hydrothermal and solvothermal strategies

Hydrothermal synthesis is a solution-based method involving the reaction of the precursor with an aqueous solution in a steel pressure vessel known as the autoclave at high temperature and
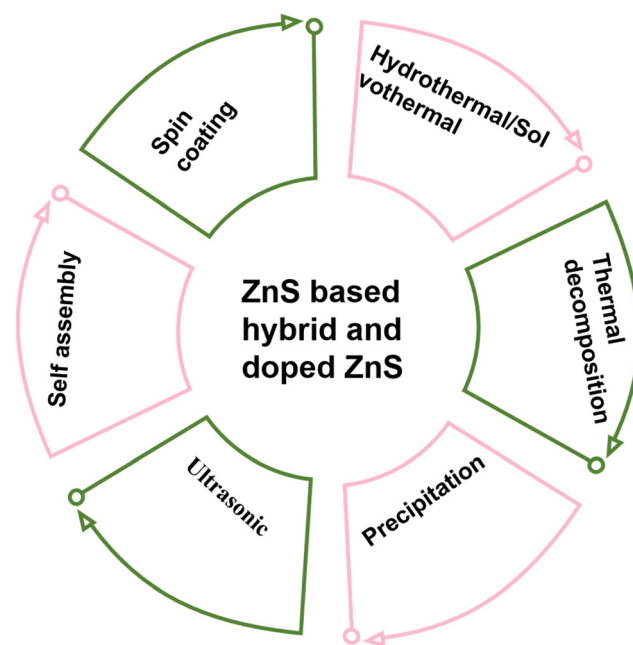

Fig. 2 The different methods of synthesizing ZnS and its heterostructures for CO_2 reduction.

pressure leading to the formation of nanocrystals.[25] In the autoclave, there is a temperature gradient at the opposite ends of the growth chamber so that the hotter end dissolves the precursor and at the cooler end, seed crystals are deposited. Similar to hydrothermal methods, solvothermal synthesis employs the same technique but with a non-aqueous solvent. The advantages of this method are that the high temperature and pressure will enhance the dissolution of precursors that will not dissolve ordinarily at the boiling point of water, thus leading to pyrolysis, and NPs with high crystallinity and monodisperse size can be obtained. Some of the disadvantages are that it is not possible to observe the reaction progress while the reaction is going on, and hence there could be safety issues in the course of the reaction, and the autoclave is very expensive. Notably, ZnS and ternary sulfide, $ZnIn_2S_4$ (ZIS), have been studied and have also been combined with other materials to form nanocomposites and heterostructures using the hydrothermal method, leading to the evolution of new compounds with fine tunable morphologies and interesting properties.[26] A summary of the studies done using the hydrothermal/solvothermal method for the synthesis of doped ZnS and composites is presented in Table 1. The findings revealed that the composites and doped ZnS materials showed better optical properties and performances than the pristine ZnS material. This has been attributed to the larger surface area, which provides many active sites for reaction to take place. The better catalytic performance is driven by the hydrothermal and solvothermal methods, which make use of high temperatures to produce stable and uniform composites with desirable morphological and optical properties. For instance, the ZnS/$ZnIn_2S_4$ heterostructure prepared by the hydrothermal method had a larger Brunauer–Emmett–Teller (BET) surface area with layered structure compared with other reported template-free ZIS samples, which in turn led to strong selectivity for CO_2 adsorption due to the availability of more active sites for the reaction to take place.[27] Furthermore, it was found that the $CuZnSnS_4$/g-C_3N_4 heterojunction demonstrated a mesoporous structure with better absorption in the visible region when compared with the pristine g-C_3N_4 material.[28]

2.2 Ultrasonication assisted synthesis

Ultrasonication is the application of sound wave vibrational energy to facilitate a chemical reaction. The method is based on the impact of acoustic cavitation, which can be described as the sequential formation (nucleation), growth (expansion), and collapse of bubbles in a tiny hot energy spot when the ultrasonic power heats the solution, leading to the production of high temperature and pressure in a few seconds that drives the chemical reaction to synthesize nanoparticles.[45,46] Ultrasonication-assisted synthesis has the advantage of being environmental benign as only little energy and time is required compared to other methods of synthesis. The ultrasonic method can cause exfoliation revealing morphologies like nanosheets with exposed active sites for enhanced CO_2 reduction. However, there is a limitation of not being able to scale up the production.

Self-supported cobalt phthalocyanine (CoPc) anchored on $ZnIn_2S_4$ nanoarrays (ZIS-CoPc) used for electrochemical CO_2 reduction was synthesized by the ultrasonic treatment.[47] ZIS was prepared by reacting thioacetamide (TAA) with zinc chloride and indium chloride with the solution adjusted to a pH of 2 and then sonicated at 85 °C for 24 h. The resulting ZIS was added to cobalt phthalocyanine (which was dissolved in diethylenetriamine) and then placed in a sonicator at 85 °C for 24 h. XPS of ZIS-CoPc showed a shift to lower binding energy compared to pure $ZnIn_2S_4$, suggesting that there is an interaction between ZIS and CoPc, which was further supported by the ICP ES analysis with Co of about 0.75 wt%. Furthermore, enhanced photocatalytic performance of the $BiFeO_3$@ZnS coated membrane, which was fabricated by the ultrasonic treatment and spraying on the PES membrane, was observed.[48] This enhanced performance was supported by the SEM analysis, which revealed ZnS as nanosheets that covered the surface of $BiFeO_3$ and the eventual coating on polyethersulfone (PES) to form a membrane with a smooth and homogenous layer without any defects. In another research, hexagonal ZIS nanosheets were fabricated by one-pot exfoliation of prepared ZIS in iso-propanol and sonicated for 5 h.[49]

2.3 Precipitation method

This method is a simple and convenient way of synthesizing nanoparticles from aqueous salts by the addition of a precipitant.[50] Commonly used precipitants are hydroxides, chlorides, carbonates, and oxalates. The resulting precipitates are then left to age and eventually collected through centrifugation. The factors affecting the composition, size and shape of the nanoparticles are the ratio of ions, temperature, type of salts used, pH and addition of surfactants. Although this method is cost effective and energy efficient and can produce nanoparticles on a large scale, it has the following disadvantages:

● If reactants have significantly different precipitation rates, this method becomes almost impossible.

● Impurities in the product may also precipitate, which may be difficult to remove sometimes.

● It necessitates the employment of numerous chemicals and may result in the generation of non-environmentally friendly wastes.[25]

Typical research utilizing the precipitation method has been reported. For example, zinc sulfide functionalized with ruthenium nanoparticles was prepared using sodium sulfide (ZnS-A) or thiourea (ZnS-B) as the source of sulfur. This was followed by deposition of Ru Nps through impregnation of ZnS powders with ruthenium(III) chloride on ZnS.[51] The modification of ZnS with Ru does not influence the electronic band structure significantly, but it was observed that the specific surface areas become lower after functionalizing with Ru, which was explained by the aggregation of NPs, leading to the blocking of some pores. This method can optimize pH to produce sulfur vacancies, and is one of the strategies that favors visible light harvesting as well as creating active sites for the reduction of CO_2.

Table 1 Summary of previous studies on ZnS- and doped ZnS-based heterostructures synthesized by the hydrothermal and solvothermal methods

S/N	Synthesized material	Morphology	Phase	BET/surface area ($m^2\ g^{-1}$)	Optical properties	Ref.
1	ZnS/ZIS	Flower-like microspheres	Hexagonal ZIS but with cubic ZnS for S-vacancies		Absorption wavelength: S vacant-ZnS/ZIS = 5 33 nm ZnS/ZIS = 513 nm	29
2	ZnS/ZIS	ZnS nanoparticles (25–35 nm) and ZIS nanosheets (40–50 nm)	Cubic ZnS and hexagonal ZIS	ZnS = 34.6 ZIS = 184.7 ZnS/ZIS = 158	Band energy gap (eV): ZnS = 3.51 ZnS/ZIS = 2.69 ZIS = 2.43	30
3	TiO_2/ZIS	ZIS – spherical shape (a diameter of 3 μm) and TiO_2/ZIS junction = 400–500 nm spheres	Anatase and ZIS	TiO_2 = 67.4 TiO_2/ZIS-S = 81.0	TiO_2/ZIS-S showed distinct red shift of the absorption edge greater than ZIS	31
4	TiO_2/ZIS	TiO_2 – nanotubes (an inner diameter of 4.94 nm) and ZIS – hexagonal structure	Hexagonal ZIS	TiO_2/ZIS = 94.90 ZIS = 71.04	TiO_2/ZIS has a greater absorbance than ZIS; decay lifetime (ns): ZIS = 1.12 TiO2/ZIS = 0.269	32
5	UCNPs/ZIS	UCNPs – regular hexagonal nanoparticles and ZIS – hierarchical nanorods	UCNPs and ZIS	Not reported	Absorption edge: ZIS = 600 nm UCNPs/ZIS = 980 nm	33
6	CNO/ZIS	Nanosheets	CNO and hexagonal ZIS	CNO/ZIS = 50 pure ZIS = 17	PL lifetimes (ns): CNO = 1.81 CNO/ZIS = 1.88 band energy gap (eV): CNO = 2.82 CNO/ZIS = 2.19	34
7	CZTS-CN	CZTS has rose-like nanoplates and NPs (100–150 nm diameter) and CZTS–CN hybrid composite has rose-like CZTS NPs evenly dispersed on the surface of CN	Graphite and kesterite CZTS	CZTS/CN = 38.46 m^2 pure CTZS = 13.9	CZTS-CN showed a wider light absorption region in the visible spectrum	35
8	TiO_2/CZTS	Agglomerated	Kesterite CZTS and anatase TiO_2	CZTS = 87.46 TiO_2/CZTS = 105.31	TiO_2/CZTS showed stronger absorption in the range 350–800 nm	36
9	CZTS-ZnO	ZnO nanorods dispersed on CZTS aggregates	Wurtzite and kesterite		CZTS-ZnO samples showed light absorption in the visible range (400–700 nm)	37
10	CIZS/carboxylated g-C_3N_4 (CNN)	Nanosheets	Cubic CIZS and graphite carbon nitride	CNN = 81.93 CIZS/CNN = 43.12	Band energy gap (eV): CNN = 2.82 CIZS/CNN = 1.66 PL lifetimes (ns): CNN = 5.13 CIZS/CNN = 20.28	38
11	Graphene/$Zn_{0.5}Cd_{0.5}S$	Hierarchical nanospheres of ZnS with graphene sheets	ZnS with a slight shift to smaller angles due to CdS	Graphene/$Zn_{0.5}Cd_{0.5}S$ = 24	Enhanced light absorption in the 700–900 nm range	39
12	ZnS/SnS_2/CdS	Dodecahedron	Cubic ZnS and SnS_2	ZnS/SnS_2/CdS = 86.5	ZnS/SnS_2/CdS showed enhanced absorption in the visible region	26
13	$Cd_{0.2}Zn_{0.8}S$/UiO-66-NH_2	$Cd_{0.2}Zn_{0.8}S$ NPs on the surface of the UiO-66-NH_2 cubes	ZnS with a slight shift to smaller angles due to CdS	$Cd_{0.2}Zn_{0.8}S$/UiO-66-NH_2 = 266 $Cd_{0.2}Zn_{0.8}S$ = 85.2	Composite has absorption edges of longer wavelengths compared to UiO-66-NH_2.	40
14	$Cd_{0.2}Zn_{0.8}S$@Ti_3C_2 (CZS@TC)	CZS NPs on TC nanosheets	ZnS with a shift in the angle due to CdS and Ti_3C_2		Band energy gap (eV): CZS = 2.86 CZS@TC = 2.49 The absorption band edge shifts to the visible and infrared region, maximum with CZS@TC with 7 wt% TiC	41
15	Cu-doped ZnS	Irregular plate-like shape	Sphalerite and wurtzite	Not reported	Cu-doped ZnS – absorption above 600 nm	42
16	Ni-doped ZnS	Agglomerated NPs	Zinc blende, ZnS, with a slight shift to the left due to Ni	ZnS = 126.6 Ni doped ZnS = 12.1	Ni doped – extended region of absorption in the visible region	43
17	ZnS	TU-ZnS – aggregated nanoparticles (~30 nm) and TAA-ZnS – interconnected coral-like microstructure	Cubic ZnS and hexagonal ZnO	Not reported	Not reported	44

UCNPs – upconversion nanoparticles, CNO – oxygen-doped carbon nitride, CZTS-CN – Cu_2ZnSnS_4-carbon nitride, CIZS – CuInZnS, CNN – carbon nitride nanosheets, and CZS – $Cd_{0.2}Zn_{0.8}S$.

In addition, Ni doped ZnS photocatalysts were prepared by the reaction between sodium sulfide, zinc sulphate and different concentrations of nickel sulphate and then left overnight under stirring.[52] The optimized photocatalyst having better light absorption contains the lowest concentration of Ni (0.1%). Precipitation followed by annealing was investigated on Ni-doped ZnS (0.2 mol% Ni) prepared by the reaction between zinc nitrate, nickel nitrate and sodium sulfide at room temperature.[53] The precipitate was washed and annealed at 500 °C for 2 h under argon and the resulting product was coupled with Ru-complex catalysts by adsorption. It was found that there is no significant difference in optical properties before and after modification of the Ru-complex onto the semiconductor.

Furthermore, $Zn_{0.5}Cd_{0.5}S$ was prepared by precipitating zinc chloride and cadmium nitrate with sodium sulfide and then optimized by acid treatment. The acid treated sample was found to have enhanced photocatalytic properties, which is due to the phase transition from the sphalerite to wurtzite structure, leading to an increase in the amount of sulfur vacancies after treating with acid.[54] The effect of sodium citrate on the morphology of Cd doped ZnS was investigated.[55] $Cd_{0.8}Zn_{0.2}S$ was prepared at 60 °C in an oil bath giving rise to 3D hierarchical flowers and nanoparticles with and without citrate respectively. The flower has a higher BET value and it showed an increased photocatalytic performance. Interestingly, a perovskite oxide, $KCa_2Nb_3O_{10}$, has been combined with different amounts of ZIS and TAA at 80 °C for 2 h to form a 2D/2D nanosheet heterojunction (ZIS/KCNO). It was found that the optimized sample has a lower ZIS content (20%-ZIS/KCNO).[56]

2.4 Self-assembly method

Self-assembly is a process in which a disordered system of preexisting components builds itself into an organized structure as a result of non-covalent interactions in a spontaneous manner. The mechanism behind self-assembly is based on variations in the orientation of particles due to Brownian motion compared to thermal energy.[50,57] Thermal energy affects the formation of soft materials at the nanoscale when the intermolecular forces are broken, thus enabling the system to reach thermodynamic equilibrium, and due to the weakness of the intermolecular interactions, it is possible to change variables such as pH or temperature, leading to phase transitions and orderliness. Some of the advantages include: low cost, simple deposition on a large-area substrate and easy modulation of energy and surface properties. One of the limitations could be during its application procedure as it might not be able to withstand lots of frictions because it is only a few nm thick. The self-assembly method allows the production of a thin layer of nanosheet material, which in turn promotes close contact for the CO_2 reduction to take place on the surface of the photocatalyst, thus enhancing better performance.

Preparation of a ternary heterojunction Z-scheme $Zn_xCd_{1-x}S/Au@g\text{-}C_3N_4$ (ZCS/Au@CN) involved a hydrothermal method followed by photodeposition of Au on ZCS and the eventual ZCS/Au@CN composite was obtained via a dual-plot

self-assembly method by first exfoliating C_3N_4 powder by ultra-sonication for 1 h, followed by the addition of the AuNPs to ZCS nanosphere dispersion and stirring at room temperature for 24 h.[58] Energy-dispersive X-ray spectrometer mapping data showed that all the elements were present and evenly distributed, which was also corroborated by XPS analysis; shifts to lower binding energies indicate chemical interaction between ZCS and CN. Similarly, a self-assembled photocatalyst was prepared using a cobalt complex and $CuInS_2/ZnS$ quantum dots by ultrasonic treatment at room temperature for 8 h and its formation was confirmed by the appearance of characteristic peaks using FTIR.[59] Also, the hybrid photocatalyst $TiO_2@CdS/ZnS$ was obtained via a self-assembly growth method by mixing hollow titanium dioxide with cadmium nitrate, zinc nitrate and thiourea with continuous stirring for 10 min after which it was refluxed at 120 °C for 5 h.[60]

2.5 Thermal decomposition method

Thermal decomposition is also known as thermolysis and it is the application of heat to break the bonds in a compound into its constituent atoms/ions.[61] It could involve the use of solvent or solventless systems. In solventless systems, a solid precursor containing metal cations, molecular ions or an organometallic compound is placed in a furnace with or without a capping agent and heated beyond its decomposition temperature, while the one with solvent involves heating precursors in a high boiling point organic solvent placed in a round bottom flask usually in the presence of a capping agent. Although the solventless method reduces the use of toxic chemicals, synthesising a nanomaterial with desired composition, structure, morphology, or even properties in a predicted way is difficult to control.[62] The use of solvents on the other hand makes it possible to prepare nanomaterials with different shapes, sizes and compositions. For instance, magnetite NPs with different morphologies were obtained by varying the volume of the solvent; a change from nanocubes to flower like morphology was observed with increase in solvent concentration.[63] The thermal decomposition is a relatively cheaper method for the production of high yield and quality materials. One of the disadvantages is the low dispersibility of the nanomaterials in aqueous medium for those applications that require water solubility.[64]

N doped porous carbon supported ZnS has been synthesized by thermolysis of a protein–Zn(II) network formed by the reaction between different amounts of $ZnCl_2$ and bovine serum albumin (BSA).[65] The optimal catalyst prepared from 2.25 : 1 $ZnCl_2$ and BSA exhibit a distinctive porous structure and good photothermal performance. In another research, it was found that different temperatures produced different phases of dual doped ZnS. $(CuGa)_{0.5}ZnS_2$ was obtained at 800 °C and $CuGaS_2$ at 600 °C in 10 h.[66] The metal organic framework (MOF) has also been thermally decomposed to produce a ZnS@ZnO heterostructure.[67] The MOF was obtained by the reaction between 2-methylimidazole, Zn nitrate and sodium sulfide, which was then subjected to heat treatment at 350 °C for 3 h to get a porous ZnS@ZnO heterostructure as evident from the

adsorption isotherm measurement, which exhibited a typical type IV plot. It was observed that the use of high temperature in the thermal decomposition method could lead to the formation of a porous structure with enhanced surface area needed for the active reaction.

2.6 Spin coating

It is a common method to prepare uniform and homogeneous thin films on the substrates using the concept of centripetal force and surface tension of the solution. It involves dropping a solution of the material onto the center of the substrate that is already spinning (dynamic spin coating) or is spun after deposition (static spin coating).[68] The spinning takes a few seconds at a high speed and during this process, the solvent evaporates to leave the material on the substrate as a thin film. The subsequent layer can then be added and the thickness formed is controlled by the spinning speed, viscosity of solvent and concentration of the solution. Some of the advantages include low cost and easy formation of uniform films. Some of the limitations of this method are: the use of multiple substrates is not possible, as the size of the substrate increases, the high-speed spinning becomes difficult, and it wastes solution.[69]

Quaternary sulfide of Cu_2ZnSnS_4 (CZTS) was fabricated through spin coating and annealing in an inert gas atmosphere.[70] Spin coating was conducted at 3000 rpm for 10 s, followed by heating at 280 °C for 20 min in air on a hot plate and then annealing at 400 °C for 20 min on a hot plate in a glove box filled with nitrogen gas. All the Raman peaks are assigned to the pristine CZTS solid solution, indicating the formation of no other metal sulfide component and this was supported by the elemental analysis performed using ICP and XRF. Our research revealed that spin coating has not been fully explored for the synthesis of ZnS in the application of CO_2 reduction; however a few research studies have shown that spin coating has been used for the fabrication of CdSe@ZnS quantum dot films with enhanced light emitting device (LED) performance[71] and also copper doped ZnS with remarkable photoluminescence properties.[72] These findings suggest that the spin coating is a viable method that should be explored.

Based on the above findings, the formation of sulfur vacancies enhances the performance of the heterostructures due to the creation of more active sites or the promotion of hole separation during photocatalysis. The morphology also plays an important role in the light harvesting properties of these nanocomposites/heterostructures. It is worth mentioning that the optimum performance is also determined by the ratios of the composition or percentage of dopants used in the preparation of the nanocomposite as well as the reaction time and temperature.

3. ZnS- and doped ZnS-based nanocomposites for CO_2 conversion

Semiconductor materials like ZnS have inherent advantages in catalysis, as they possess electronic structures that facilitate charge transfer and redox reactions. When exposed to various forms of energy, such as light or electrical current, ZnS can generate electron–hole pairs, setting the stage for electrochemical, photochemical, or photothermal reactions. This unique capability positions ZnS and doped ZnS as versatile candidates for CO_2 conversion, and they offer several distinct advantages:

• Efficient charge separation: the electronic band structure of ZnS allows for efficient separation of photoexcited charge carriers, which is crucial for promoting catalytic reactions. The ability to separate electrons and holes reduces recombination, enhancing the overall catalytic efficiency.

• Tunable properties: through careful engineering and doping with specific elements, the electronic and optical properties of ZnS can be tailored to optimize its performance in different CO_2 conversion processes.

• Sustainability: ZnS is an environmentally friendly and non-toxic material, aligning with the principles of green chemistry. Its low environmental impact makes it an attractive option for sustainable CO_2 reduction technologies.

Researchers are making great progress toward creating sustainable and effective CO_2 conversion solutions by utilizing the intrinsic qualities of these semiconductor materials. These remedies could play a significant role in lessening the consequences of climate change and promoting future generations that are more ecologically sensitive.

3.1 Electrocatalytic ZnS-based heterostructures

A simple answer to the energy and environmental crises is the electrochemical conversion of CO_2 into compounds with additional value. CO_2 reduction has slow reaction kinetics, and so effective and durable electrocatalysts are crucial for speeding up this process. Utilizing renewable electricity to reduce CO_2 to CO and then create value-added products is a crucial technical strategy for achieving CO_2 resource efficiency. There has been a lot of buzz recently about electrocatalysis based on ZnS heterostructures, which could convert CO_2 into more valuable chemicals. ZnS, a semiconductor material with a suitable bandgap, offers a promising platform for electrocatalytic CO_2 reduction. The electrocatalytic properties of ZnS are primarily attributed to its electronic structure, which allows for efficient charge transfer and redox reactions.

By adding heteroatoms, functional groups, and adions to catalysts, it is possible to successfully tune their adsorption energy and increase their inherent properties for CO_2 reduction. Doping ZnS with various elements, such as nitrogen, sulfur, or transition metals, can further enhance its electrocatalytic performance. Doping alters the electronic properties of ZnS, leading to improved charge separation, increased active sites, and better catalytic selectivity. For example, nitrogen-doped ZnS has shown excellent CO_2 reduction activity with improved faradaic efficiency.

Recent advances in the development of ZnS-based electrocatalysts have focused on optimizing the morphology, size, and structure of ZnS nanomaterials to maximize their surface area and expose more active sites. This can be achieved through the synthesis of ZnS nanowires, nanoparticles, or other

nanostructures. The combination of efficient charge transfer and specific surface design makes ZnS-based electrocatalysts highly promising for CO_2 reduction in sustainable energy applications. According to Song *et al.*[20] ZnS nanoparticles were affixed to a ZnO surface, resulting in the formation of a stable ZnS/ZnO interface structure. Compared to a reversible hydrogen electrode (RHE), the ZnS/ZnO interface exhibited a significant density and a high CO faradaic efficiency and maintained stability for a duration of 40 h. These properties led to its notable electrocatalytic CO_2 reduction performance.

Non-precious metals, such as zinc, copper, and silver, have been found to be promising catalysts for reducing carbon dioxide. Their electron-rich characteristics, however, result in poor performance for CO_2 reduction and weak adsorption of reaction intermediates. Consequently, Zn nanosheets covered with a porous ZnS subnanometer layer, a fundamentally novel electrocatalyst, have been shown by Li *et al.*[73] to achieve high catalytic performance that is on par with noble metallic catalysts. Both theoretical and experimental studies show that the ZnS subnanometer layer functions similarly to S dopants, appropriately alters Zn catalyst adsorption, and ultimately achieves high catalytic activity. In the meantime, the ZnS subnanometer layer offers long-term durability since, in contrast to S doping, it is chemically inert during the reduction of CO_2.

The practical implementation of CO_2 electroreduction technology is limited by the absence of high-performance electrode materials. Zhen *et al.*[74] used the sulfur infiltration approach to create a ZnS/Zn electrode in an attempt to address this issue. This technique is a sophisticated surface treatment technology. A notable advantage of constructing a ZnS/Zn electrode *via* sulfur infiltration is the creation of a translation layer connecting the ZnS layer and Zn substrate. This occurs due to the infiltration of sulfur atoms through the Zn substrate. The ZnS layer therefore does not exfoliate from the Zn substrate due to the strong bond that ZnS forms with the Zn substrate. ZnS/Zn has been investigated as a potential cathode for CO_2 electroreduction in propylene carbonate/tetrabutylammonium perchlorate (PC/TBAP) within a membrane electrolysis cell. The potentiostatic electrolysis current density remains constant at 6.72 mA cm^{-2} at a voltage of 2.4 V, and the faradaic efficiency of CO formation approaches 92%. In comparison to the Zn electrode, the ZnS/Zn electrode exhibits a greater catalytic activity. The electrolysis cell with two compartments is illustrated in Fig. 3(a). The anode of the cell is a stream of 99.99% pure graphite rod, which has a length of 15 cm and a diameter of 5 mm. The cathode is a ZnS/Zn sheet with a diameter of 1 cm. The reference electrode, I_3^-/I^-, has 0.1 M tetrabutylammonium iodide (Bu_4NI) and 0.05 M iodine (I_2). The reference electrode was calibrated using ferrocene as the internal standard. To construct the reference electrode, a platinum wire was dipped into the reference solution. The ionic process ($I_2 + I^- = I_3^-$) produced {0.05 M I_3^- and 0.05 M I^-}, which are indeed present in the reference solution. To avoid contamination, a salt bridge was used to maintain the separation of the catholyte and reference solution within the cell. Teflon was used to join
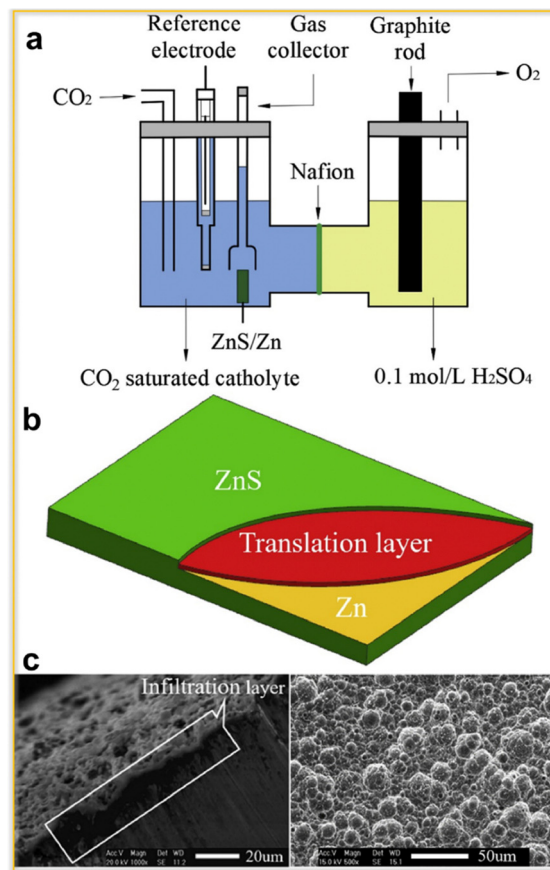

Fig. 3 (a) An organic electrolyte-based two-compartment electrolysis cell, (b) an infiltration layer schematic and (c) a scanning electron micrograph of a ZnS electrode.[75]

and seal the reference electrode and salt bridge. The ZnS/Zn electrode produced by the infiltration technique has a three-layered structure (Fig. 3(b)), with Zn serving as the substrate and the top layer. A translation layer sits between the two of them. This transition layer is readily apparent under a scanning electron microscope (Fig. 3(c)). The translation layer is essential for correctly attaching ZnS to the substrate. Because the infiltration layer sticks to the substrate firmly and is challenging to remove, the infiltration approach is better than other methods like electrochemical and deposition. The ZnS/Zn electrode's surface morphology was investigated using SEM (Fig. 3(c)). There are several spherical embossments on the ZnS/Zn electrode surface, each with an average size of 9 mm. Consequently, a big surface area is possible. By decreasing CO_2, a significant degree of surface roughness contributes to an increase in current density. Therefore, the infiltration of S element into the metal substrate is a feasible method for creating the ZnS/Zn electrode.

3.2 Photocatalytic ZnS-based heterostructures

The photocatalytic CO_2 reduction process (CO_2RR) on a heterogeneous catalyst offers a feasible way to produce renewable carbonaceous fuels at room temperature and pressure using
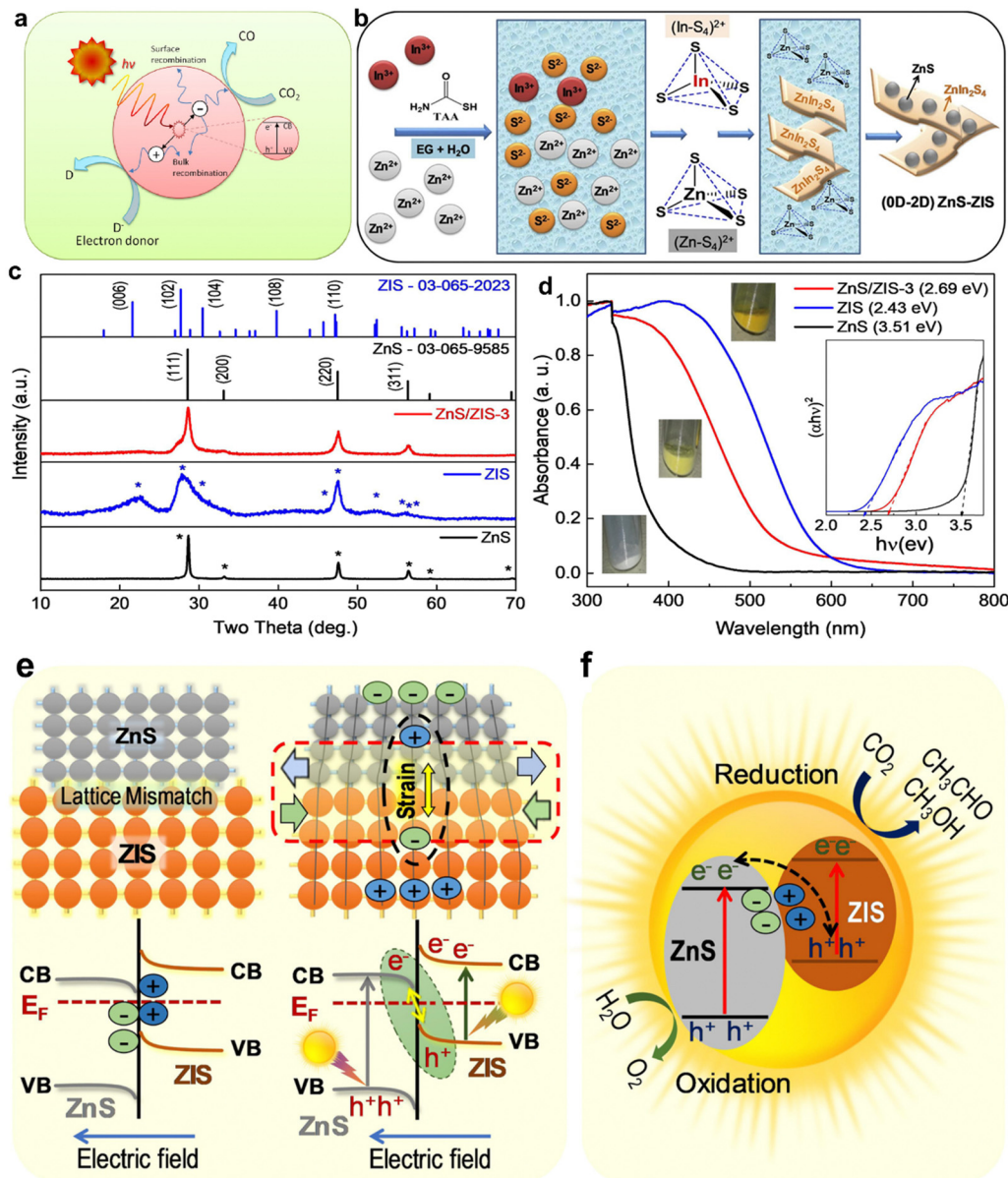
Fig. 4 (a) Schematic diagram of photoexcitation and electron transfer processes. Formation mechanism, crystal structure, and optical properties of the (0D−2D) ZnS−ZIS composite. (b) Formation process. (c) XRD patterns and (d) UV-vis diffuse reflectance spectra and (inset) Tauc plots with direct fitting for cubic ZnS, hexagonal ZIS, and the ZnS/ZIS-3 composite.[30] (e) Schematic illustration of lattice mismatch and strain effect between cubic ZnS and hexagonal ZIS phases in ZnS/ZIS-3. (f) Direct Z-scheme of ZnS/ZIS (n−n+) heterojunction in ZnS/ZIS-3.

solar light as the only energy source. It also presents the chance of reducing CO_2 emissions. Photophysical and photochemical processes interact intricately during photocatalytic CO_2 conversion. Photoexcitation, which starts this conversion, occurs when photons with energy equivalent to or greater than the semiconductor's band gap are absorbed by a photocatalyst. Electrons are excited from the valence band (VB) to the conduction band (CB) as a result of this absorption. In contrast to the CB, which is the lowest empty band, the VB is the highest energy band filled with electrons in their ground state. Intraband transitions occur between the excited electrons and the generated holes, as seen in Fig. 4(a). Through radiative or non-radiative paths, these charge carriers can go to the surface of the semiconductor or recombine at trap sites. The destiny of these charge carriers plays a vital role in establishing the photocatalytic process efficiency. The excited electrons can reach the semiconductor surface if recombination proceeds more slowly than surface reactions. In this instance, they interact with adsorbed species to enable CO_2 reduction. Because it reduces CO_2 and produces useful solar fuels, this interaction is essential for the photocatalytic conversion process. For photocatalytic CO_2 conversion to be effective, a balance between charge carrier recombination and surface reaction participation is therefore essential.

ZnS heterostructure photocatalysis has become a powerful tool for utilizing solar energy to propel CO_2 conversion into useful compounds and fuels. Because of its appropriate bandgap, light absorption qualities, and capacity to produce electron–hole pairs in response to light, zinc sulfide (ZnS) has outstanding photocatalytic activities. When photons with energy over ZnS's bandgap are absorbed, electron–hole pairs are created and this forms the basis for zinc sulfide's photocatalytic mechanism. The photoexcited electrons can contribute to the reduction of CO_2 to form compounds based on carbon. Good photocatalysis depends on ensuring that these charge carriers are used appropriately for CO_2 conversion and are not lost through recombination.

Doping ZnS with elements like nitrogen or metal ions can enhance its photocatalytic activity by facilitating charge separation and preventing electron–hole recombination. Moreover, heterostructures composed of ZnS coupled with other semiconductors, such as TiO_2 or ZnO, can create favorable interfaces for charge transfer and promote photocatalytic CO_2 reduction. These heterostructures often lead to enhanced catalytic activity due to their synergistic effects.

In order to obtain better performance, recent research has concentrated on improving the synthesis of ZnS-based photocatalysts, regulating their size and shape and customizing their surface features. According to Koci et al.[76] the reactor shape affects CO_2 photocatalytic reduction as well. An important part of the search for sustainable energy solutions is the development of ZnS heterostructures, which offer a potential path for increasing the efficiency of CO_2 conversion under visible light.

Excellent electron transportability and energy band compatibility are displayed by ZnO and ZnS. The heterostructure of ZnO–ZnS is investigated using transmission electron microscopy (TEM), energy dispersive spectroscopy (EDS), and X-ray photoelectron spectroscopy (XPS). The ZnO–ZnS heterojunction NW array creation mechanism is a result of a combination of a substitution reaction and a regular dissolution crystallization process. Compared to pure ZnO NW arrays, the composites' heterostructure and the electron transport path from ZnS to ZnO enable much greater photocatalytic activity. Further experiment revealed a significant drop in CO_2, which was ascribed to the combined effects of the incorporated Pt NPs and the ZnO–ZnS heterostructure.

Monodispersed Ni-doped ZnS (ZnS:Ni) nanocrystals in an aqueous colloidal form are effective visible light-responsive CO_2RR photocatalysts, according to Pang et al.[23] The wavelength-dependent quantum yield suggests that Ni doping is a key factor in visible light activity. ZnS:Ni (0.1%) colloidal nanocrystals that have been altered by Cd^{2+} show an amazing 5.6% quantum efficiency at 420 nm and a high selectivity of >95% for HCOOH production.

In their groundbreaking research, Sabbah et al.[30] have pioneered the use of direct Z-scheme semiconductor heterostructures in photocatalysis for the conversion of CO_2 into solar fuels. This approach notably enhances charge carrier separation and effectively isolates redox processes. The team successfully synthesized a $ZnS/ZnIn_2S_4$ heterostructure, comprising hexagonal $ZnIn_2S_4$ (ZIS) nanosheets and cubic ZnS nanocrystals, through a single-pot hydrothermal method, as depicted in Fig. 4(b). This heterostructure is characterized by microstrain at the interface, which generates an electric field conducive to the Z-scheme mechanism. Remarkably, the $ZnS/ZnIn_2S_4$ composite achieves an exceptional photochemical quantum efficiency of about 0.8% at an optimal Zn : In ratio of approximately 1 : 0.5. This efficiency is nearly 200-fold greater than that of pristine ZnS. The electronic levels and band alignments of this composite were meticulously analyzed using UV-vis and ultraviolet photoemission spectroscopy. Further insights into the direct Z-scheme and carrier dynamics were obtained through photoluminescence (PL), time-resolved PL, and photo-reduction experiments. Additionally, the adsorption of CO_2 and related intermediate species on the catalyst during the photocatalytic reaction was investigated using diffuse-reflectance infrared Fourier transform spectroscopy. This innovative direct Z-scheme mechanism, facilitated by microstrain, heralds a new era in the development of CO_2 reduction photocatalysts, potentially revolutionizing the field of sustainable energy. Fig. 4(c) displays the powder XRD patterns of the ZnS, ZIS, and ZnS/ZIS-3 composite samples that were produced. Using UV-vis diffusive reflectance spectroscopy, the light-harvesting capacities of ZnS, ZnS/ZIS-3, and ZIS photocatalysts were determined, as seen in Fig. 4(d). The absorption edge of ZnS was approximately 350 nm, whereas that of ZIS was approximately 520–550 nm. The optical response of the composites blue shifted in comparison to that of virgin ZIS as the ZnS content rose. The associated colors varied from white to light yellow and deep yellow, as shown by the approximate direct bandgaps of 3.51, 2.69, and 2.43 eV for ZnS, ZnS/ZIS-3, and ZIS, respectively, as seen in the Tauc plot in the inset of Fig. 4(d). Notably, ZnS has a tail from 500 to 350 nm in the UV-vis band. All things considered, the photocatalytic CO_2 reduction mechanism of a ZnS/ZIS-3 direct Z-scheme heterostructure has been demonstrated, as observed in Fig. 4(e) and (f).

3.3 Photothermal ZnS-based heterostructures

Photothermal catalysis involving ZnS heterostructures represents a unique and innovative approach for CO_2 conversion. When exposed to the right light wavelengths, zinc sulfide (ZnS) can effectively produce localized heat due to its significant absorption of visible and near-infrared light. It is possible to use this photothermal effect for catalytic CO_2 reduction.

By converting the absorbed light energy into heat, photothermal catalysis speeds up chemical reactions, such as the reduction of CO_2. By lowering the activation energy of the process, heat produced by ZnS nanoparticles can encourage CO_2 molecules to adsorb and to be activated on the catalytic surface. Reaction rates and selectivity rise as a result. ZnS can be further doped with certain elements or combined with other nanomaterials to improve its photothermal characteristics. The photothermal response and catalytic activity for CO_2 conversion are largely dependent on the dopant selection and composite structure design.
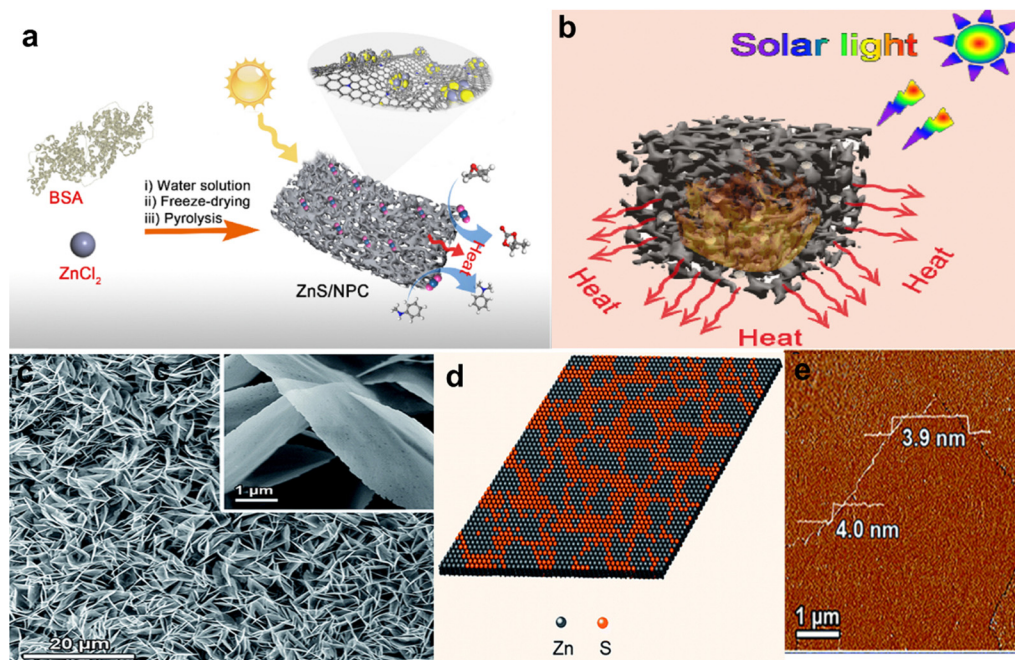
Fig. 5 (a) Schematic illustration of the preparation of ZnS/NPC-*X* for catalytic conversion of CO₂, by pyrolyzing protein–Zn(II) networks. (b) Schematic illustration of the photothermal effect of ZnS/NPC-*X* (c)–(e) Characterization of S–Zn–S NSs. (c) SEM image; inset shows a typical single nanosheet. (d) Schematic map of the structure of S–Zn–S NSs. (e) AFM image.[73]

Using photothermal catalysis to reduce CO_2 has a number of benefits, such as high energy efficiency, adaptability to mild reaction conditions, and possibility of using sunlight as an energy source. This strategy creates new opportunities for energy-efficient and sustainable CO_2 conversion solutions. Tang *et al.*[77] synthesized N-doped porous carbon-supported ultra-small ZnS (ZnS/NPC-*X*) as photothermal catalysts for CO_2 conversion by pyrolyzing the protein–Zn(II) network. Fig. 5(a) and (b) shows a schematic representation of the photothermal action of ZnS/NPC-*X*. The primary catalyst ZnS/NPC-2 shows exceptional photothermal catalytic performance for CO_2 cycloaddition and methylation processes due to its hierarchical porous structure, high photothermal efficiency, and abundant Lewis acid/base sites.

The creative effort of Li *et al.*[73] produced a novel catalyst for CO_2 reduction by cleverly adding a stable, discrete subnanometer layer of ZnS on the surface of Zn nanosheets. Thermal evaporation was used to create S–Zn–S nanosheets (NSs) on a fluorine-doped tin oxide (FTO) glass substrate in order to accomplish this alteration. Scanning electron microscopy (SEM) analysis of the resultant structure shown in Fig. 5(c) reveals that it is made up of dense arrays of NSs that are developed on the FTO substrate and have lateral sizes of several microns. Atomic force microscopy (AFM) analysis, as demonstrated in Fig. 5(d), reveals that these NSs have an average thickness of about 4 nm. It is noteworthy that the S–Zn–S NS catalyst exhibits remarkable stability together with great faradaic efficiency. Its performance is comparable to that of noble metal catalysts and exceeds all previously documented Zn-based catalysts. The special function of sulfur atoms in the S–Zn–S NSs is responsible for this improved performance. By efficiently altering the Zn nanosheet, these sulfur atoms maximize the adsorption of the *COOH intermediate. This change is essential because it suppresses the competitive hydrogen evolution reaction while also facilitating CO_2 reduction. The Zn nanosheets are symmetrically changed with a ZnS passivation shell layer (PSL) on both sides, according to the results, which are described in Fig. 5(e). Compared to conventional elemental doping, this discrete subnanometer layer method has several advantages, especially in terms of high catalytic activity and long-term durability. Additionally, this catalyst's straightforward synthesis procedure indicates that it might be used to improve other inexpensive metal materials, opening the door for the creation of extremely stable and active CO_2 reduction catalysts.

3.4 Structure–performance relationships of ZnS-based catalysts for CO_2 reduction

The efficacy of ZnS-based catalysts in CO_2 reduction processes is significantly influenced by their structural characteristics, such as doping, morphology, cocatalysts, and surface area.[78–80] Each of these elements plays a crucial role in dictating the catalyst's catalytic activity and stability. Introducing heteroatoms such as nitrogen into ZnS modifies its electronic properties and can greatly enhance catalytic performance. Studies, such as those conducted by Pang *et al.*,[52] have shown that nitrogen-doped ZnS offers higher catalytic activity and selectivity towards CO_2 reduction compared to its undoped counterpart. Nitrogen doping creates additional acceptor levels within the ZnS band structure, enhancing charge separation and

reducing electron–hole recombination, thereby facilitating more effective photocatalytic reduction of CO_2 to carbon monoxide and other hydrocarbons under visible light. The size and morphology of ZnS nanostructures critically determine their performance due to the impact on the surface-to-volume ratio. Li *et al.*[81] reported that ZnS nanoparticles with diameters between 5 and 10 nm displayed increased active sites and stronger CO_2 adsorption capabilities, leading to superior photocatalytic performance. These nanoparticles exhibit quantum size effects that enhance light absorption and modify electronic properties, thereby boosting photocatalytic activity. A larger surface area of ZnS catalysts enhances the dispersion of reactants and intermediates, thereby improving reaction kinetics. According to Zhou and Guzman[82] ZnS nanosheets with extensive surface areas provide improved CO_2 adsorption, which is crucial for higher conversion rates during the reduction process.

4. Mechanism of CO_2 transformation using ZnS-based materials

The chemical reduction of greenhouse gases such as CO_2 into hydrocarbon-based fuels, for example methanol, is essential due to the nonrenewable nature of their natural sources, which include crude oil, coal and natural gas, and these sources of energy are depleting due to their constant use.[83] Research interest has grown in the area of reduction of CO_2 to liquid fuels using photocatalysts,[84,85] and this is important because of the benefit of reducing the amount of CO_2 available globally by converting it into useful materials. In light of this, the underlying mechanism under which the successful reduction of CO_2 into useful liquid fuels occurs is worth reviewing.

4.1 Photocatalytic mechanisms of CO_2 transformation using ZnS-based materials

In general, when a photocatalyst is exposed to UV light that comes with incident energy that is greater than its energy gap, there is a transition of free electrons (e^-) from the valence band (VB) into the conduction band (CB). At this instance, the free e^- are excited into the CB and positively charged holes (h^+) are created in the VB. This leads to the accumulation of the electrons in the CB. The electrons in the CB can take part in a reduction reaction, whereas the holes can take part in an oxidation reaction. Similar to photosynthesis, photo-induced reactions can take place on the surface of the photocatalyst.[86] Such interesting reactions that can occur on the surface of the photocatalyst are as a result of the holes and electrons that are generated in the process. The electron released can take part in the dissociation of molecules of water to produce hydrogen gas, reduce CO_2 to hydrocarbon fuels and involve in the production of free oxygen radicals from oxygen molecules with strong oxidizing ability. The holes, however, can take part in the oxidation of water to form oxygen molecules and hydroxyl radicals and can also convert organic pollutants into CO_2 and H_2O.[87,88]
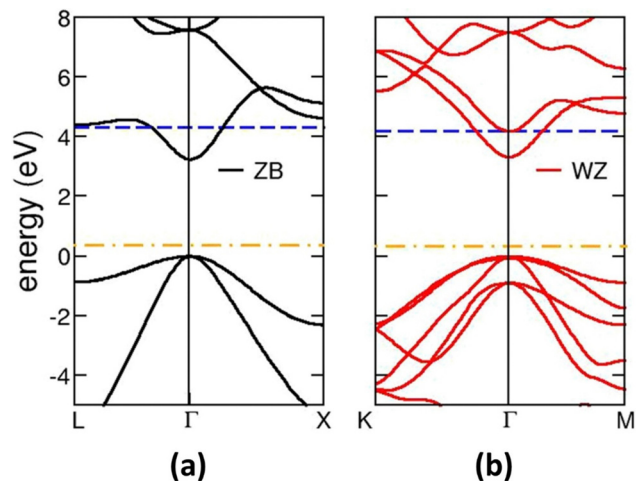

Fig. 6 Band structures of the two forms of ZnS: (a) zinc blende and (b) wurtzite.

Furthermore, the efficiency of a photocatalytic material mainly depends on the type of material it is made up of. The energy values of the CB and VB influence the photocatalytic properties of the photocatalyst, and this in turn can affect the efficiency of the photocatalyst. Finally, an excellent photocatalyst should be environmentally friendly and should have high photostability.[89] The rate of movement of charges within the photocatalytic material is important since the rate with which the holes can migrate is slower than that of the electrons by approximately 2–4 times, making the electron extraction difficult even when photo-induced electrons are transmitting constantly. As a result, it is believed that removing holes is a critical stage that influences how successfully O_2 and H_2 are liberated. Fig. 6 shows that ZnS exists in two distinct forms of ZnS with almost the same band structures and this is evident from their band gaps. The band gap of wurtzite (WZ) is 3.77 eV and that of zinc blende (ZB) is 3.72 eV.[90,91] These band gaps are wide, which is important because during the photoreaction, the electrons and holes are rapidly generated.[92]

However, because ZnS is an inexpensive, environmentally friendly, and readily available semiconductor, it is known to be a potential material for photocatalytic reduction of CO_2. The
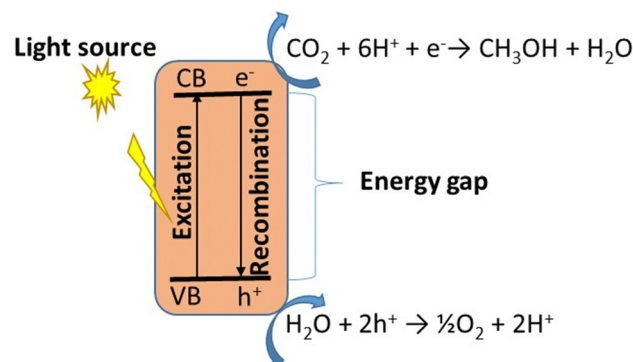

Fig. 7 Schematic representation of a single photocatalyst.

issue with ZnS is that its sensitivity to UV radiation is not compensated for by its inability to detect visible light, resulting in inefficient utilization of solar energy.[90] To add, as a single semiconductor material, ZnS possesses an intrinsic ability to rapidly recombine the electrons and holes that are generated under UV irradiation, and this also reduces its photocatalytic efficiency. The mechanism by which this occurs is illustrated in Fig. 7, where a single photocatalyst that is irradiated with light enables the reduction of CO_2 to CH_3OH by the electrons that are generated. The holes are, however, involved in the oxidation of water to oxygen gas.[84,93] The electron that is generated during the excitation process is used to reduce CO_2 to methanol, while the holes facilitate the generation of oxygen.

Many studies have been conducted to improve the sensitivity of ZnS to visible light, such as element doping,[94–96] vacancy defect engineering,[97,98] and decorating with noble metals.[99,100] Since the aforementioned approaches are expensive and difficult to control, attention has shifted to the formulation of ZnS-based heterostructures, which tend to possess a much better photocatalytic ability.[88,101] Photocatalysts that are made up of two or more types of semiconductors are preferable to those with a single component. This is because they are known to exhibit a much higher catalytic efficiency and have a broad absorption range, high photostability and strong redox ability. This is owing to the interaction between the charges that are formed during light irradiation; holes in the first semiconductor interact with the electrons in the second, through a channel that is usually formed between them. A significant redox ability of the photocatalyst is observed when the energy gaps of the two semiconductors are similar. This, however, is due to the excellent ability of the heterojunction photocatalysts to increase the spatial separation of electron–hole pairs.[102] A heterojunction is the contact between two distinct semiconductors with different band structures, which can result in band

alignment.[103] For example, when ZnS is coupled with WO_3, the photocatalytic ability of the coupled system is observed to be better than those of the individual semiconductors. WO_3 is a well-known component of a Z-scheme photocatalyst because it is active towards UV light.[104] It has a wide band gap that lies between 2.4 and 2.7 eV.[105] Heterojunctions are classified into three types: type I, type II, and type III. A type I heterojunction, also known as a straddling band gap heterojunction, occurs when the energy of the CB of one component, B, is lower than that of the other component, A, and the energy of the VB of B is higher than that of A. This is shown schematically in Fig. 8(a). This arrangement implies that electrons and holes will move from component A and accumulate in component B under light irradiation. The electrons and holes that are generated may not split since the charges are now on B. However, redox reactions can still occur on the component of the photocatalyst heterostructure with the smaller redox potential. If the CB and VB of semiconductor A are greater than those of semiconductor B, a type II heterojunction, also known as a staggered band gap heterojunction, is created. This leads to the migration of electrons from component A to B and the corresponding migration of holes from component B to A when irradiated with light. This results in the spatial separation of electron–hole charge pairs. Reduction occurs in component B with a lower reduction potential, while oxidation takes place on A with a lower oxidation potential (Fig. 8(b)). A type III heterojunction, also known as a broken band gap heterojunction, occurs when the CB and VB of component A are higher than B, in so much that the band gaps of the two components do not align (Fig. 8(c)). As a consequence, when irradiated with light, the migration of electrons and holes and the spatial separation of the electron–hole pair cannot occur. There is yet another type of photocatalyst known as the direct Z-scheme heterojunction. It is so called because of the mechanism of migration of
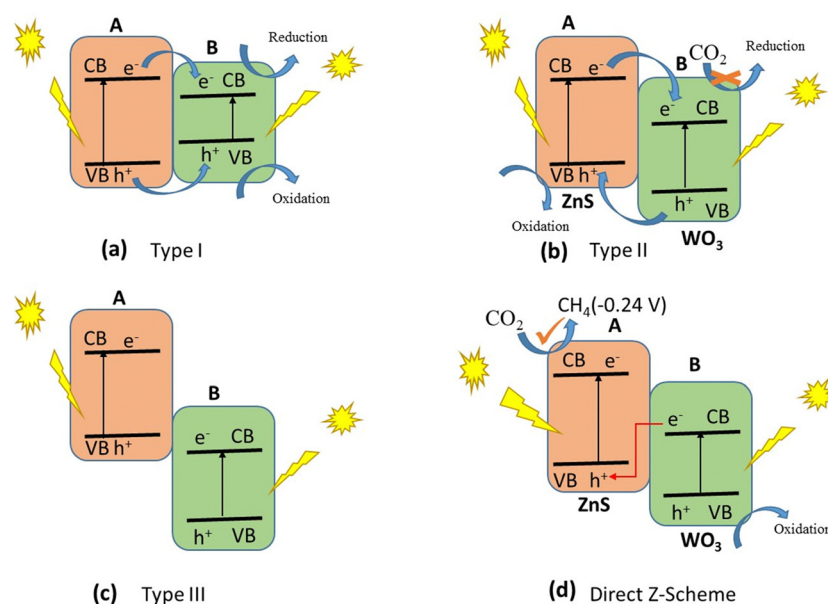

Fig. 8 The mechanism of photocatalytic CO_2 reduction on ZnS/WO_3 heterojunctions as they respond to light radiation is depicted schematically.
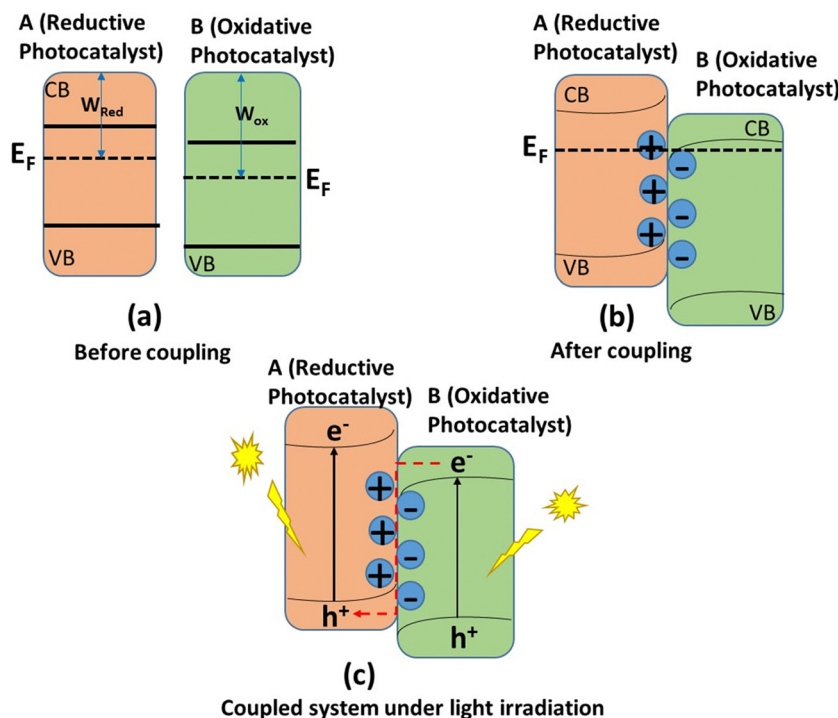
Fig. 9 The mechanism of direct Z-scheme photocatalyst production using oxidative and reductive semiconductors, showing the band structures (a) before and (b) after coupling. (c) The band structure of a linked system under light irradiation. The Fermi energy level is denoted by the symbol E_F.

electrons, mostly from component B to A, in a path that resembles letter "Z", as can be seen in Fig. 8(d). The arrangement of a direct Z-scheme heterojunction appears to be the same as that of a type II heterojunction.

4.2 Direct Z-scheme and Z-scheme mechanisms of CO₂ transformation using ZnS-based materials

To fully understand the mechanism of direct Z-scheme formation, it is important to remember that the development of a heterojunction between two photocatalysts is linked to their band structures and Fermi levels. The oxidative photocatalyst must have a lower Fermi level than the reductive photocatalyst for this mechanism to work,[93] as can be seen in Fig. 9. When the two photocatalysts are coupled, electrons will migrate from the reductive photocatalyst to the oxidative photocatalyst so that the Fermi levels of the two photocatalysts can arrive at equilibrium.[106] As a result of this charge migration, an internal electric field will develop in such a way that the direction of the field moves from the reductive photocatalyst to the oxidative photocatalyst.[107]

Since the direct Z-scheme photocatalyst greatly enhances the spatial charge separation and provides a better photocatalytic efficiency than the type-II heterojunction, and the architectures of the two photocatalysts are similar, some characterization techniques are needed to differentiate between the two. Such characterization techniques, which are based on charge migration, include the photocatalytic CO₂ reduction, X-ray photoelectron spectroscopy (XPS), and photodecomposition of metal nanoparticles, among others. Photocatalytic reduction of CO₂

into useful fuel products entails a series of steps, with each step having its own reduction potential (Table 2). If a specific step is required to get a given product, the photocatalyst must have a lower reduction potential than the corresponding standard redox potential for that step of the reaction. The product of the CO₂ reduction can give insight into the photocatalyst on which electrons that are photogenerated reside more.[108]

To corroborate this, Murillo-Sierra et al.[104] synthesized a direct Z-scheme photocatalyst consisting of WO_3 and ZnS components and applied it in the conversion of CO_2 present in water vapor for the production of propane and propylene. Maximum production of the hydrocarbons was obtained when 5 wt% WO_3 was used. This ensured continuous generation of enough electrons and holes, which are then migrated from the direct Z-scheme surface to CO_2 to form the C_1–C_3 hydrocarbons. Other ratios that were used are WO_3(10%)/ZnS and WO_3(20%)/ZnS, but did not give better results when compared with the WO_3(5%)/ZnS ratio. Furthermore, the interface energy of the WO_3(001)/ZnS($\bar{1}\bar{1}\bar{1}$) slab was calculated to be -0.985 J m^{-2}, an indication of thermodynamically stable

Table 2 The standard redox potential (E_0 vs. NHE at pH 7) for CO_2 conversion. Adapted from ref. 109–111

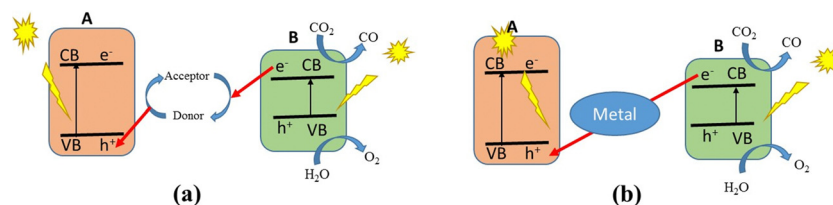| Reduction reaction	E^0 (V) vs. NHE at pH = 7
$CO_2 + 2H^+ + 2e^- \rightarrow HCOOH$	-0.61
$CO_2 + 2H^+ + 2e^- \rightarrow CO + H_2O$	-0.53
$CO_2 + 4H^+ + 4e^- \rightarrow HCHO + H_2O$	-0.48
$CO_2 + 6H^+ + 6e^- \rightarrow CH_3OH + H_2O$	-0.38
$CO_2 + 8H^+ + 8e^- \rightarrow CH_4 + 2H_2O$	-0.24

Fig. 10 A schematic of a Z-scheme photocatalyst displaying (a) a liquid-phase Z-scheme and (b) a solid-phase Z-scheme.

interface. In another experiment, Sabbah et al.[30] prepared nanocrystals of ZnS and coupled them with $ZnIn_2S_4$ nanosheets to form a heterostructure. The formation of the direct Z scheme was investigated by testing it in the reduction of CO_2 to solar fuel. This was supported by photoluminescence and time-resolved photoluminescence experiments. Furthermore, Zhou and Guzman[112] also reported the use of colloidal ZnS suspension for use as a photocatalyst in the conversion of CO_2 to formate ($HCOO^-$). This was possible when the incident UV light was maintained at 345 nm. The energy of electronic excitation from the VB to the CB was calculated to be 3.59 eV, and the CO_2 reduction was reported to occur at a potential of -1.04 V vs. NHE. The results obtained also showed that the surface carriers were active below 10 ms for the transfer of electrons and below 215 ms for the loss of holes, demonstrating that the reactive carriers can be detected within longer time scales than the range that is usually explored during time-resolved spectroscopy. This shows that the colloidal suspension of the ZnS photocatalyst in the presence of Na_2S is very efficient for the direct reduction of CO_2 to $HCOO^-$.

For Z-scheme photocatalysts, the electron–hole pairs are photogenerated sequentially when two photocatalysts are connected in series with a redox mediator and made up of an electron pair donor/acceptor, as illustrated in Fig. 10.

The first photocatalyst, usually the one that possesses a higher band gap, absorbs the incident UV light and generates electrons and holes. Upon light irradiation on a Z-scheme that is made of a liquid-phase photocatalyst, the electrons on the oxidative photocatalyst are picked up by the acceptor component of the redox mediator and transferred to the donor, as given in equation (1):

$$Acceptor + e^- \rightarrow Donor \qquad (1)$$

The holes on the other hand are picked up by the donor component of the photocatalyst and are transferred to the acceptor, as can be seen in equation (2):

$$Donor + h^+ \rightarrow Acceptor \qquad (2)$$

The benefits of the presence of the redox mediator are that excess charge pairs that are photogenerated are removed by reacting with the acceptor/donor pair. However, a few drawbacks abound:

(i) There is a possibility for a back reaction to occur since the acceptor/donor pair can also react in the opposite direction.

(ii) It can only be used in liquid medium, restricting its use in other photocatalytic states.

It is reported that the inclusion of a redox mediator drastically improves charge separation and the ability of the ZnS based photocatalyst to respond to light.[113,114] For example, Zhou et al.[115] investigated the formation a Z-scheme photocatalyst that is composed of ZnS and NH_2-MIL-125(Ti), with carbon based quantum dots as a redox mediator, using the electron spin resonance (ESR) method. As a result of the successful interaction involving the electrons and the LUMO of NH_2-MIL-125(Ti) and the holes in the VB of the ZnS, more electrons were observed to accumulate in the CB of the ZnS, as measured using ESR. This confirmed the formation of the Z-scheme heterostructure. Meanwhile, Yoshino et al.[116] prepared three photocatalytic systems of $CuGaS_2$ using solid-state reaction and flux methods. The photocatalyst with the $(CuGa)_{0.5}ZnS_2$ ratio, prepared by the flux method, was demonstrated to be the most efficient, selective and stable photocatalyst for CO_2 reduction. In order to investigate the formation of the Z-scheme photocatalyst, the bare $(CuGa)_{0.5}ZnS_2$ photocatalyst made using reflux was coupled with the $CoO_x/BiVO_4$ photocatalyst and used in the reduction of CO_2. The two photocatalysts were connected by reduced graphene oxide (RGO), a solid-state electron mediator. The integrity of the Z-scheme photocatalytic system was ensured by X-ray diffraction (XRD), diffuse reflectance spectroscopy (DRS), atomic emission spectroscopy (AES) and ESR. They observed that the light-induced holes on the metal sulfide were continuously used up by the light-induced electrons on $BiVO_4$ through electron transfer via RGO resulting in steady CO_2 reduction by the Z-scheme system. The commonly used redox mediators in the reduction of CO_2 by the ZnS Z-scheme heterojunction photocatalyst are presented in Table 3.

4.3 S-scheme mechanisms of CO_2 transformation using ZnS-based materials

The "S-scheme photocatalyst" works in the absence of a redox mediator. The charges are generated simultaneously by

Table 3 Common redox mediators for CO_2 conversion by ZnS Z-scheme heterojunction photocatalysts

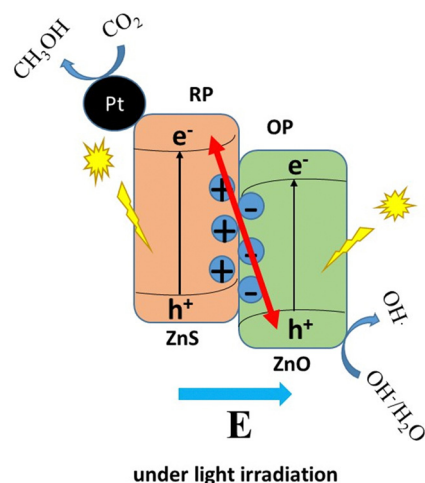| Photocatalyst	Synthesis method	Redox mediator	Ref.
ZnS/Rgo/Bi$_2$S$_3$	Hydrothermal	Reduced graphite oxide	117
ZnS/ZnO	Air annealing	ZnS$_x$O$_{1-x}$/defect mediated	118
ZnS/g-C$_3$N$_4$	Hydrothermal	Co$_9$S$_8$/defect mediated	119
ZnS/NH$_2$_MIL-125(Ti)	One pot	Carbon quantum dots	115

Fig. 11 Diagrammatic representation of the S-scheme mechanism of the photogenerated charge carrier transfer process, where $\vec{E}$ denotes the electric field's direction. Drawn from scholarly sources (Mohamed *et al.*, 2021).

excitation of the two photocatalysts, connected in parallel with each other. The two semiconductors used have different band gaps.[120] The schematic representation of the S-scheme is given in Fig. 11, which shows that the reductive photocatalyst possesses greater CB and VB positions and a lower Fermi level than the oxidative photocatalyst. When the two photocatalysts are coupled, there is an observed spontaneous migration of the electrons from the reductive photocatalyst to the oxidative photocatalyst. This automatically creates electron depletion and accumulation layers.[121] Consequently, the photocatalyst causes the reduction process to occur by acquiring a positive charge, while that causing oxidation to occur acquires a negative charge. At the same time, an internal electric field is generated that points in the direction of the oxidative photocatalyst. This enables the photo-induced electrons to migrate from the oxidative photocatalyst to the reductive photocatalyst. At this point, the coulombic attraction between the two charges causes the photogenerated electrons in the CB of the oxidative photocatalyst and the holes in the VB of the reductive photocatalyst to recombine at the interface between the two photocatalysts.[122,123] Hence, the three driving forces that influence the operation of the S-scheme photocatalyst include internal electric field, band bending, and coulombic attraction.

The advantages of the S-scheme are the following;

(i) The useless electron–hole pairs are removed through recombination.

(ii) The photo-induced electrons in the CB of the reductive photocatalyst and the holes in the VB of the oxidative photocatalyst are used for photocatalytic reactions.

The formation and application of a mesoporous PtZnO/ZnS S-scheme heterojunction for efficient reduction of CO_2 to CH_3OH was demonstrated by Mohamed *et al.*[124] Upon exposure of the photocatalyst to UV light, the electrons migrated and populated the CB of both ZnS and ZnO, and the corresponding holes accumulated on the VB of both ZnS and ZnO. Owing to the fact that the CB of ZnO is less than that of ZnS, the photogenerated electrons in ZnS immediately migrate to the platinum nanoparticles (Fig. 11). Some of the S-scheme heterojunctions of ZnS used in the conversion of CO_2 are given in Table 4.

5. The stability of ZnS catalysts for CO_2 reduction

Zinc sulfide (ZnS), both in its unmodified form and when doped with various heteroatoms, has shown considerable promise as a catalyst for CO_2 reduction.[128] However, the practical application of these catalysts in sustainable energy solutions critically depends on their stability during operation. Several degradation mechanisms affect the performance of ZnS catalysts during CO_2 reduction, including photocorrosion, sintering of nanoparticles, and poisoning of active sites by reaction intermediates or environmental contaminants.[129] Photocorrosion, in particular, poses a significant challenge, as it leads to the dissolution of ZnS under illumination, resulting in the loss of catalytic activity. Moreover, the reactivity of photoexcited carriers can further degrade the catalyst through reactions with water or oxygen. Adsorbed water on ZnS surfaces is crucial for photocorrosion, with even less than 0.1 wt% H_2O being sufficient to initiate Zn^0 formation, as indicated by various studies, including those concerning UV irradiation effects on aqueous ZnS suspensions.[130] Photocorrosion often evidenced by the darkening of ZnS occurs rapidly upon exposure to UV light, with numerous Zn^0 nuclei appearing within seconds and causing a marked decrease in reflectance. The formation of these nuclei predominantly along structural defects in the crystal matrix indicates a vulnerability at these sites due to excess strain energy, enhancing reactivity and water adsorptivity. Further studies conducted by Weide *et al.*[131] delineated the photocorrosion pathway under oxygen-free conditions, revealing the production of various compounds, including elemental Zn and S, $ZnSO_4$, and $Zn(OH)_2$, with a significant hydrogen to

Table 4 Some studies on ZnS heterostructures for CO_2 conversion using S-scheme heterojunctions

Heterojunction	Characterization techniques	Application	Year	Ref.
ZnS/ZnO	XRD, XPS, EIS	Conversion of CO_2 to CH_3OH	2021	124
ZnS/ZnIn$_2$S$_4$	S-scheme	H_2 evolution and CO_2 reduction	2022	125
ZnIn$_2$S$_4$/g-C$_3$N$_4$	EPR, XPS	CO_2 conversion to CO	2022	126
ZnO/ZnIn$_2$S$_4$	FTIR, discrete Fourier transform, ESR, PL, TRPL	Conversion of CO_2 to CO and CH_4	2023	127

XRD = X-ray diffraction; XPS = X-ray photoelectron spectroscopy; EIS = electrochemical impedance spectroscopy; EPR = electron paramagnetic resonance spectroscopy; FTIR = Fourier transform infrared; ESR = electron spin resonance; PL = photoluminescence; and TRPL = time-resolved photoluminescence

zinc sulfate molar ratio. The initial dissociation into Zn and S due to UV-generated electron–hole pairs, followed by hydrolysis of nascent sulfur, forms H_2S and H_2SO_4, indicating that water molecules slightly dissociate, adsorb, and lower the energy barrier for these reactions. The valence and conduction band edge potentials of ZnS suggest that only the reduction of dissolved zinc ions is thermodynamically feasible under illuminated conditions; yet, experimental data suggest that this needs critical reevaluation as actual band edge potentials could differ. Notably, the presence of oxygen significantly accelerates photocorrosion, with $ZnSO_4$ being the primary corrosion product in oxygenated environments, highlighting the complex dynamics of photocatalytic reactions involving ZnS.[132]

To mitigate these degradation processes, contemporary advancements in materials science have introduced ZnS-based heterostructures and composites. Coating ZnS with protective layers of inert materials, such as graphene or titanium dioxide, has proven effective in shielding the catalyst from degradative environmental factors.[133] Additionally, embedding ZnS within metal–organic frameworks (MOFs) or hybrid polymeric matrices can confer structural stability and mitigate zinc atom leaching. Alterations to the electronic properties of ZnS through doping with metals like silver or copper, or non-metals such as nitrogen, have also enhanced resistance to photocorrosion and chemical wear.[134] These dopants introduce new energy levels within the bandgap of ZnS, facilitating improved charge separation and transfer, thereby diminishing the likelihood of side reactions that contribute to catalyst degradation. Empirical studies and pilot implementations have further elucidated the operational stability of ZnS catalysts under industrial conditions. Notably, nitrogen-doped ZnS has sustained high catalytic activity over prolonged durations in photoelectrochemical setups dedicated to CO_2 reduction.[135] Likewise, ZnS/ZnO heterostructures have exhibited commendable stability in continuous flow reactors, underscoring their potential for scalability in industrial applications.[136]

Future research efforts are poised to deepen the understanding of factors influencing ZnS catalyst stability. Utilization of advanced *in situ* characterization techniques, such as X-ray diffraction (XRD) and electron microscopy, will allow real-time monitoring of structural transformations in ZnS catalysts during operational deployment. Insights gleaned from these studies are anticipated to drive the development of next-generation ZnS catalysts characterized by enhanced stability and efficacy, thereby facilitating their integration into the matrix of sustainable energy technologies.

6. Computational models of ZnS and ZnS heterojunctions

Over the years, computational models based on density functional theory (DFT) have proven to be of immense benefit in the study of reactions on surfaces, particularly those that hitherto were unachievable in the laboratory or those whose mechanisms were difficult to unravel.[137–139] It is well known that

competitive hydrogen evolution frequently occurs with photocatalytic CO_2 reduction. For instance, Li *et al.*[81] used a combination of experimental and DFT methodologies to solve the mystery surrounding the selectivity of H_2 evolution over CO_2 photoreduction utilizing a ZnS nanocatalyst that is made up of heterojunctions. The approach they used included a combination of both dynamics (adsorption/desorption of reactants/products) and thermodynamics (redox potential and change in Gibbs free energy of significant intermediates). The authors also demonstrated that the obtained ZnS nanoparticle photocatalyst for CO_2 reduction showed a higher hydrogen evolution reaction selectivity than the CO_2 reduction reaction. The DFT calculations indicated that the adsorption energies of H_2O molecules on the clean surface of ZnS (-0.77 eV) are lower than those of CO_2 molecules (-0.54 eV) and that the adsorption energies of CO molecules (-0.19 eV) are significantly lower than those of H_2 molecules. A larger negative number, on the other hand, indicates that the adsorbate is more easily adsorbed on a solid surface, because the adsorption energy value measures the degree of surface adsorption. As a result, CO is significantly more difficult to desorb from the ZnS surface than CO_2, and H_2O is more easily adsorbed on the ZnS surface than CO_2. Furthermore, the successful doping of Ni into the crystal lattice of ZnS revealed enhanced photocatalytic ability because the projected density of state (PDOS) revealed that a new state was created, which extended the range of absorption to the visible light region.

Some of the important properties of ZnS and ZnS heterostructures that are usually calculated are: geometric structure, band structure, density of state (DOS), molecular orbitals, and work function.[140–142] For example, Di Liberto *et al.*[101] optimized the structure of the ZnS(110)/TiO$_2$(001) heterostructure and got a lattice vector of $a = 5.443$ Å. The calculated band gap (E_g) gave a value of 4.29 eV, with the relativistic effect pushing the E_g to a higher value by 0.1 eV. The electronic structures of single ZnS and CdS photocatalysts and the linked $Zn_xCd_{1-x}S$ system were studied.[139] According to the computed band structures, the energy gaps are 2.115 eV, 1.369 eV, and 1.167 eV, respectively (Fig. 12). The authors contended that photoinduced electrons might be transmitted through the d-orbitals of the Pt atom, resulting in faster charge transfer and separation kinetics. However, the calculated charge density further confirms that electrons are concentrated on the d-orbital of the Pt metal.

In another study, Yan *et al.*[143] performed DFT geometry relaxation using generalized gradient approximation with Perdew–Burke–Ernzerhof on the heterostructure of ZnS(110)/Bi$_2$WO$_6$(100). Some of the electronic properties of the heterostructure that were calculated include a good optical sensitivity band gap value of 2.537 eV. The DOS and projected density of states (PDOS) showed that the formation of the heterojunction caused the 3d electrons in Zn to move from the lower level of the VB to the shallow level. The DFT calculation revealed that the range of light absorption of the photocatalytic material was extended to 600 nm. Performing similar DFT calculations, howbeit with the Vienna *Ab initio* Simulation Package (VASP), Pang *et al.*[52] demonstrated that the theoretical results obtained
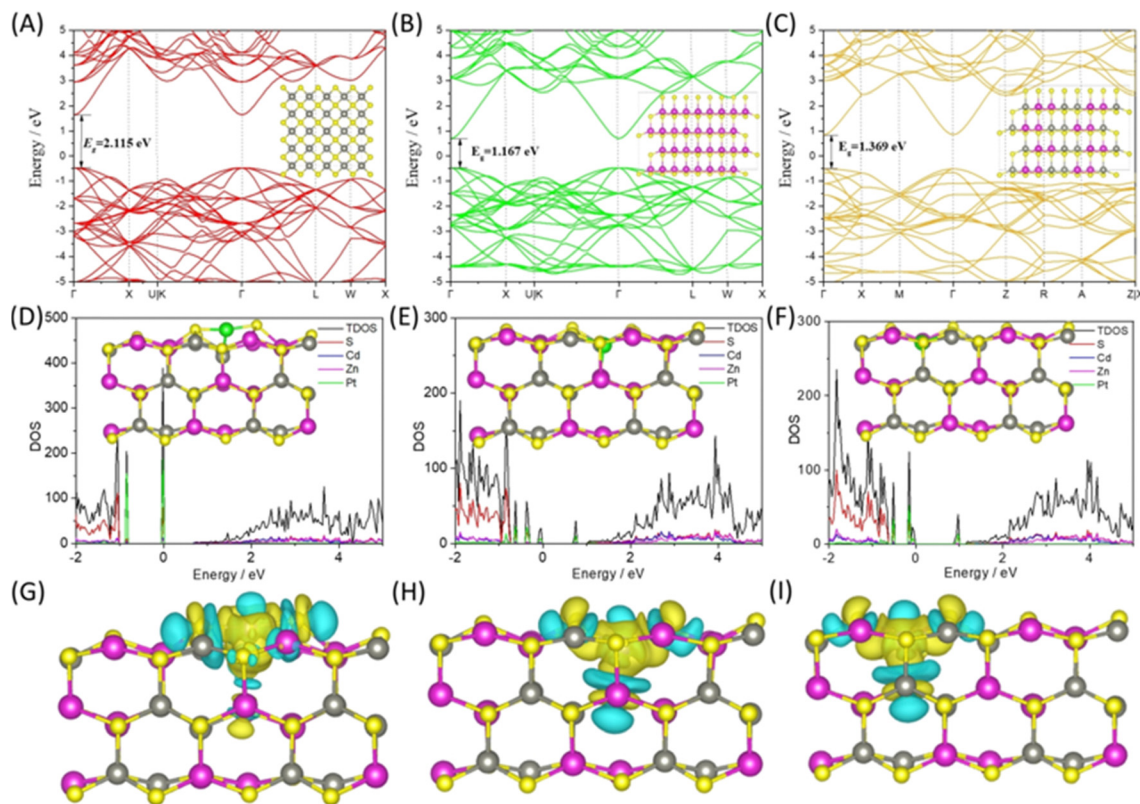
Fig. 12 The electronic structures of (A) ZnS, (B) CdS, and (C) $Zn_xCd_{1-x}S$ are shown (the gray, pink, and yellow spheres represent Zn, Cd, and S atoms, respectively). The work functions of (D) ZnxCd1@xS-Pt1, (E) ZnxCd1@xS-Pt1 (Zn), (F) ZnxCd1@xS-Pt1 (Cd). (G), (H), and (I) indicate the DOSs and charge density differences.[139]

corroborate those of the experiment that sulfur vacancies enhance the CO_2 reduction reaction. Ni doping of the structure increases the electronic energy band position (Fig. 13(a) and (b)), sulfur vacancy formation (increased to 0.76 eV) and the optical absorption properties. Importantly, they reported that even though doping increased the electronic properties of the photocatalyst, the CO_2 reduction ability was greatly reduced. A summary of some of the electronic and geometric parameters of the ZnS heterostructures determined using DFT is given in Table 5.

7. Valuable chemicals/fuels obtainable from CO_2 transformation

The conversion of CO_2 into valuable chemical products is a fast-growing field that offers a dual benefit of mitigating greenhouse gas emissions while producing useful compounds. Zinc sulfide (ZnS), a semiconductor material, has shown promise as a photocatalyst, as an electrocatalyst, and as a photothermal catalyst in the reduction of CO_2 due to its favorable band gap and stability under reaction conditions. By using ZnS-based catalytic systems, several key products can be derived from the transformation/reduction reaction.

7.1 Methane

Methane (CH_4) is one of the simplest hydrocarbons and can be produced through the hydrogenation of CO_2 and a primary
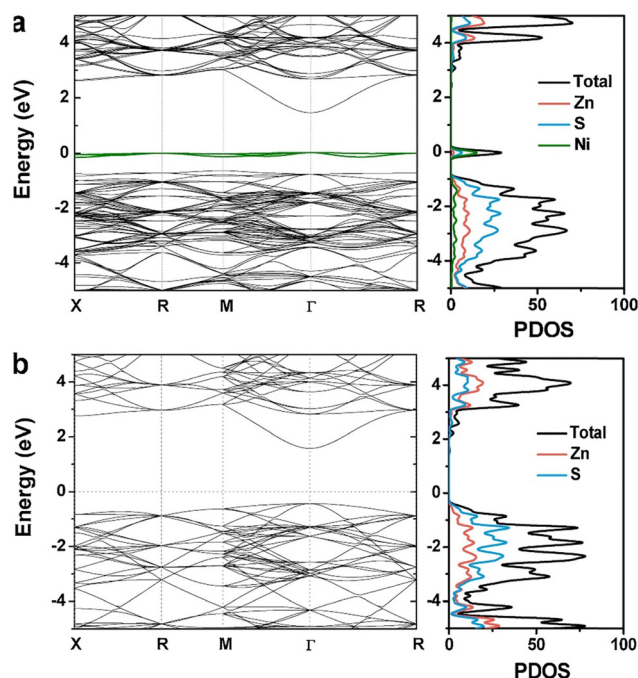
Fig. 13 The electronic band structure and the DOS; differentiated into total and partial. (a) ZnS that is 2.7% doped with Ni and (b) undoped ZnS.[52]

component of natural gas, which offers significant energy storage capabilities when produced through CO_2

Table 5 Calculated electronic and geometric properties of ZnS heterostructures determined using DFT methods for CO_2 reduction

Heterostructure	DFT functional	Pseudopotential	E_g (eV)	Geometric parameters (Å)	Ref.
$ZnS(110)/TiO_2(001)$	PBE0	Hay-Watt	4.29	$a = 5.431$ Zn–S bond length = 2.360	101
ZnS/SiO_2	PBE-D3	—	3.02	$a = 5.1$	144
Cu-doped $ZnS(001)$ & (010)	PBE	Ultrasoft	2.17	$a = b = 3.843$; $c = 6.299$	145
Copper-doped ZnS	PBE-D3	GTH & DZVP-MOLOPT-GTH	3.37	—	42
ZnO/ZnS	PBE; HSE06	—	2.24	$a = 5.74$; $b = 5.37$; $c = 24.21$	146
$ZnS(110)/NiS$	GGA-PBE	—	3.66	$a = 9.43$; $b = 6.66$	147

GTH = Goedecker–Teter–Hutter and HSE06 = Heyd–Scuseria–Ernzerhof.

conversion.[148] Utilizing ZnS-based catalysts in the photocatalytic reduction of CO_2 to methane presents an attractive method to harness renewable energy resources and reduce carbon emissions. The process is driven by the ability of ZnS to effectively absorb and utilize light, facilitating the necessary electron–hole separation that reduces CO_2 in the presence of hydrogen.[149] Research indicates that ZnS, when doped or coupled with other suitable materials, can significantly enhance the photocatalytic activity due to improved charge carrier separation and extended light absorption.[90] This reaction not only addresses environmental concerns but also provides a renewable route to methane production, which could be integrated into the existing natural gas infrastructure. Future advancements in the modification of ZnS catalysts are likely to focus on increasing efficiency, selectivity, and stability to make industrial-scale production feasible.

7.2 Ethanol

Ethanol (C_2H_5OH) is another valuable product derived from the catalytic conversion of CO_2. Ethanol production from CO_2 using ZnS-based catalysts involves converting the carbon dioxide captured from industrial flue gases into a valuable alcohol that serves both as a fuel and as an industrial solvent.[150] The catalytic reduction process utilizes the semiconductor properties of ZnS to generate reactive electron–hole pairs under UV light. These reactive species are instrumental in reducing CO_2 to ethanol, potentially in a reaction environment that includes water vapor or other hydrogen sources.[151] The practical implementation of this technology in industrial settings could significantly mitigate CO_2 emissions by converting them into ethanol, which can be used in fuel blends, thereby reducing reliance on fossil fuels. However, challenges such as improving the yield and selectivity of ethanol and the long-term stability and recyclability of the ZnS catalysts remain. Research is ongoing to optimize the reaction conditions and catalyst design, including the use of nanostructured ZnS or hybrid systems that may offer better control over the product distribution and enhance light absorption efficiency.

7.3 Alcohols

The synthesis of higher alcohols (such as methanol, propanol, and butanol) from CO_2 via ZnS-catalyzed processes expands the utility of carbon capture technologies by transforming a greenhouse gas into valuable chemical feedstocks. ZnS catalysts facilitate this conversion by utilizing their photocatalytic, electrocatalytic, and photothermal catalytic properties under the influence of the external stimuli like light irradiation, electric field or heat to initiate and drive the reduction of CO_2.[152] These alcohols are integral to various industrial applications, serving as solvents, fuels, and intermediates in chemical synthesis. The effectiveness of ZnS in these reactions often hinges on the surface properties and the electronic structure of the catalyst, which can be tuned through doping or forming composites with other materials to enhance selectivity and efficiency.[153] Advanced research explores the scalability of this approach, aiming to optimize reaction conditions and catalyst configurations to improve the economic viability of producing higher alcohols from CO_2.

7.4 Olefins

Olefins, such as ethylene and propylene, are critical for the petrochemical industry, primarily used in the production of plastics and other polymers.[154] Their synthesis from CO_2 using ZnS-based catalysts represents a groundbreaking shift towards more sustainable chemical processes. The role of ZnS in this context is to facilitate the reduction of CO_2, possibly through formation of intermediate species such as formic acid or methanol, which are further dehydrated or dehydrogenated to form olefins.[155] This process requires precise control over reaction conditions and catalyst properties to ensure high selectivity and yield. Enhancements in ZnS catalyst design, such as surface modification or the incorporation of co-catalysts, are crucial for improving the reaction kinetics and stability, thereby making the catalytic production of olefins from CO_2 a viable industrial process.

7.5 Formic acid

Formic acid (HCOOH) is another valuable chemical that can be synthesized from CO_2 conversion. Formic acid production via the ZnS-catalyzed reduction of CO_2 is an environmentally benign route that converts a potent greenhouse gas into a valuable chemical used in various industries, including agriculture, leather processing, and textile manufacturing.[156] The reaction leverages the strong reducing power generated by ZnS under UV light, electric field or heat where the catalyst induces the selective reduction of CO_2 to formic acid.[80] The efficiency of this conversion process can be significantly enhanced through the optimization of catalyst surface area, light absorption properties, and reaction environment. Developing robust, reusable ZnS catalyst systems that maintain high activity over prolonged operational periods is key to commercializing this

technology, with ongoing research focused on catalyst stability and the minimization of competing reactions.

7.6 Carbon monoxide (CO)

Carbon monoxide, though less desirable due to its toxicity, is a crucial industrial feedstock in the production of chemicals such as methanol and certain types of fuels.[157] Its generation from CO_2, catalyzed by ZnS, involves partial reduction processes where specific reaction conditions are meticulously controlled to optimize yield and selectivity. The photocatalytic properties of ZnS enable the absorption of light and facilitate the reduction of CO_2 to CO at the catalyst surface.[130] The development of this process is significant for synthesizing hydrocarbons and other chemicals from CO_2, providing a pathway to utilize CO_2 as a resource rather than treating it solely as a waste product.[158] Future developments will likely focus on enhancing the selectivity and efficiency of CO production, potentially integrating it with other processes to form a comprehensive carbon recycling strategy.

8. Conclusion and prospects

Carbon dioxide (CO_2) reduction is an imperative endeavor in the realm of environmental sustainability and combating climate change. As CO_2 levels continue to rise in the Earth's atmosphere due to industrial and anthropogenic activities, the need for effective methods to mitigate their impact on the environment has become increasingly pressing. The major routes that have been explored for the photocatalyst synthesis are the hydrothermal and solvothermal methods and it was found that the temperature and the time of reaction affect the quality of the sample produced. It will be good to explore other green methods for synthesizing the nanocomposites, such as microwave assisted synthesis under ambient conditions. Evaluating the performance of ZnS-based catalysts under varying environmental conditions, such as fluctuations in temperature, pressure, and CO_2 concentrations typical of industrial environments, will be crucial. This will help to identify any discrepancies in performance observed under laboratory conditions *versus* actual industrial settings. Furthermore, the economic and environmental impacts on scaling up ZnS-based catalysts, including cost analysis, resource availability, and potential environmental benefits or drawbacks, should be critically analyzed. This would provide a holistic view of the practical challenges and opportunities in employing ZnS-based catalysts in real-world applications, ultimately guiding their development towards commercial viability.

Moreover, the catalytic properties and mechanisms of ZnS heterostructures are being investigated with keen interest as evident from the available pool of literature. Although ZnS in any of its forms (WZ or ZB) possesses a high band gap and is highly sensitive to UV light, its sensitivity to visible light is quite low. As a consequence, many photocatalytic, electrocatalytic and photothermal materials have been employed to synergistically improve the sensitivity of ZnS heterostructures to external stimuli such as light,

electrical or heat energy for various applications, including the CO_2 reduction reaction. To this end, the understanding of the mode of operation of these heterostructures lies in the knowledge of the mechanism of their formation.

To comprehend the mechanistic behavior of the CO_2 conversion/transformation and to clarify the function of individual catalyst components, a combination of reactor experiments, thorough DFT simulations of a complex reaction network, and a multi-site first-principles microkinetic model can be examined.[159] This model can provide significant information on a computationally tractable catalyst model with new insights into the reaction behavior at various sites in the reactor and along the reactor to easily identify strategies to optimize and design appropriate reactor conditions without altering the reaction paths. Moreover, additional information on the relationships between the catalyst structure and activity is provided by microkinetic analysis, which is useful for the rational design of high-tech catalytic materials. Moreover, the properties often calculated using DFT simulations include geometric properties (lattice vectors), electronic band structures, energy gaps, energy values of the molecular orbitals, DOS (total and partial) and PDOS, which still require much work to be done particularly on the extension of the simulations to *ab initio* molecular dynamics and the calculation of their thermal properties.

The construction of a first principles detailed kinetic model for ZnS-based catalysts will enable the forecasting of catalytic performance and product profiles at desired circumstances through the use of an appropriate computational model, reaction pathways, and thermodynamic consistency analysis.

In conclusion, the transformation of CO_2 into valuable products using ZnS-based catalysts not only contributes to carbon recycling efforts, but also provides pathways to synthesize important chemical compounds and fuels. The utilization of ZnS-based catalysts enhances these processes by exploiting their catalytic properties, which are crucial for achieving high efficiency and selectivity in the conversion of CO_2. ZnS and doped ZnS-based nanocomposites offer versatile solutions for CO_2 conversion through electrocatalysis, photocatalysis, photothermal catalysis, and other innovative approaches. These materials hold the promise of addressing the critical challenge of reducing CO_2 emissions. This field is evolving rapidly, with ongoing research aimed at optimizing the performance of ZnS-based catalysts and exploring their novel applications in sustainable energy systems. The future of CO_2 reduction may well rely on the continued development and utilization of ZnS and related nanocomposites.

Data availability statement

No data were used for the research described in this article.

Conflicts of interest

The authors declare that they have no known competing financial interests or personal relationships that could have appeared to influence the work reported in this paper.

References

1 L. J. R. Nunes, The Rising Threat of Atmospheric CO_2: A Review on the Causes, Impacts, and Mitigation Strategies, *Environments*, 2023, **10**(4), 66, DOI: **10.3390/environments10040066**.

2 H. Wang, H. Jiang, H. Wang, Q. Liu and P. Huo, NiS Cocatalyst–Modified $ZnIn_2S_4$ as Ohmic-Junction Photocatalyst for Efficient Conversion of CO_2, *Energy Technol.*, 2022, **10**, 1–10, DOI: **10.1002/ente.202101158**.

3 H. Wang, X. Li, X. Zhao, C. Li, X. Song, P. Zhang and P. Huo, A review on heterogeneous photocatalysis for environmental remediation: From semiconductors to modification strategies, *Chin. J. Catal.*, 2022, **43**, 178–214, DOI: **10.1016/S1872-2067(21)63910-4**.

4 L. Wu, L. Wu, C. Guo, Y. Guan, H. Wang and J. Lu, Progress in Electroreduction of CO_2 to Form Various Fuels Based on Zn Catalysts, *Processes*, 2023, **11**, 1039, DOI: **10.3390/pr11041039**.

5 L. S. Zhan, Y. C. Wang, M. J. Liu, X. Zhao, J. Wu, X. Xiong and Y. P. Lei, Hydropathy modulation on Bi_2S_3 for enhanced electrocatalytic CO_2 reduction, *Rare Met.*, 2023, **42**, 806–812, DOI: **10.1007/s12598-022-02212-w**.

6 Z. Xiao, P. Li, H. Zhang, S. Zhang, X. Tan, F. Ye, J. Gu, J. Jun Zou and D. Wang, A comprehensive review on photo-thermal co-catalytic reduction of CO_2 to value-added chemicals, *Fuel*, 2024, **362**, 130906, DOI: **10.1016/j.fuel.2024.130906**.

7 J. Wang, S. Lin, N. Tian, T. Ma, Y. Zhang and H. Huang, Nanostructured Metal Sulfides: Classification, Modification Strategy, and Solar-Driven CO_2 Reduction Application, *Adv. Funct. Mater.*, 2021, **31**, 1–39, DOI: **10.1002/adfm.202008008**.

8 F. N. Tubiello, M. Salvatore, A. F. Ferrara, J. House, S. Federici, S. Rossi, R. Biancalani, R. D. Condor Golec, H. Jacobs, A. Flammini, P. Prosperi, P. Cardenas-Galindo, J. Schmidhuber, M. J. Sanz Sanchez, N. Srivastava and P. Smith, The Contribution of Agriculture, Forestry and other Land Use activities to Global Warming, 1990–2012, *Global Change Biol.*, 2015, **21**, 2655–2660, DOI: **10.1111/gcb.12865**.

9 Z. K. Xin, Y. J. Gao, Y. Gao, H. W. Song, J. Zhao, F. Fan, A. D. Xia, X. B. Li, C. H. Tung and L. Z. Wu, Rational Design of Dot-on-Rod Nano-Heterostructure for Photocatalytic CO_2 Reduction: Pivotal Role of Hole Transfer and Utilization, *Adv. Mater.*, 2022, **34**, 1–9, DOI: **10.1002/adma.202106662**.

10 Z. Li, J. Liu, R. Shi, G. I. N. Waterhouse, X. D. Wen and T. Zhang, Fe-Based Catalysts for the Direct Photohydrogenation of CO_2 to Value-Added Hydrocarbons, *Adv. Energy Mater.*, 2021, **11**, 1–9, DOI: **10.1002/aenm.202002783**.

11 G. Chen, R. Gao, Y. Zhao, Z. Li, G. I. N. Waterhouse, R. Shi, J. Zhao, M. Zhang, L. Shang, G. Sheng, X. Zhang, X. Wen, L. Z. Wu, C. H. Tung and T. Zhang, Alumina-Supported CoFe Alloy Catalysts Derived from Layered-Double-Hydroxide Nanosheets for Efficient Photothermal CO_2 Hydrogenation to Hydrocarbons, *Adv. Mater.*, 2018, **30**, 1–8, DOI: **10.1002/adma.201704663**.

12 Y. Shiga, N. Umezawa, N. Srinivasan, S. Koyasu, E. Sakai and M. Miyauchi, A metal sulfide photocatalyst composed of ubiquitous elements for solar hydrogen production, *Chem. Commun.*, 2016, **52**, 7470–7473, DOI: **10.1039/c6cc03199d**.

13 L. Zheng, F. Teng, X. Ye, H. Zheng and X. Fang, Photo/Electrochemical Applications of Metal Sulfide/TiO_2 Heterostructures, *Adv. Energy Mater.*, 2020, **10**, 1–32, DOI: **10.1002/aenm.201902355**.

14 W. Liu, E. Ha, L. Wang, L. Hu, L. Y. S. Lee and K. Y. Wong, Creating Multiple Parallel Internal Phase Junctions on ZnS Nanoparticles as Highly Active Catalytic Sites, *Adv. Mater. Interfaces*, 2018, **5**, 2–7, DOI: **10.1002/admi.201800611**.

15 X. Hao, Y. Wang, J. Zhou, Z. Cui, Y. Wang and Z. Zou, Zinc vacancy-promoted photocatalytic activity and photostability of ZnS for efficient visible-light-driven hydrogen evolution, *Appl. Catal., B*, 2018, **221**, 302–311, DOI: **10.1016/j.apcatb.2017.09.006**.

16 M. Zhou, S. Li, S. Wang, Z. Jiang, C. Yang, F. Guo, X. Wang and W. Kei Ho, Anchoring $ZnIn_2S_4$ nanosheets on ultrathin boron carbon nitride layers for improved photo-redox catalysis, *Appl. Surf. Sci.*, 2022, **599**, 153985, DOI: **10.1016/j.apsusc.2022.153985**.

17 Y. Zhang, N. Cao, S. Szunerits, A. Addad, P. Roussel and R. Boukherroub, Fabrication of ZnCoS nanomaterial for high energy flexible asymmetric supercapacitors, *Chem. Eng. J.*, 2019, **374**, 347–358, DOI: **10.1016/j.cej.2019.05.181**.

18 Y. Xia, B. Cheng, J. Fan, J. Yu and G. Liu, Near-infrared absorbing 2D/3D $ZnIn_2S_4$/N-doped graphene photocatalyst for highly efficient CO_2 capture and photocatalytic reduction, *Sci. China Mater.*, 2020, **63**, 552–565, DOI: **10.1007/s40843-019-1234-x**.

19 H. Peng, D. Liu, X. Zheng and X. Fu, N-doped carbon-coated ZnS with sulfur-vacancy defect for enhanced photocatalytic activity in the visible light region, *Nanomaterials*, 2019, **9**(12), 1657, DOI: **10.3390/nano9121657**.

20 Y. Song, Y. Wang, J. Shao, K. Ye, Q. Wang and G. Wang, Boosting CO_2 Electroreduction *via* Construction of a Stable ZnS/ZnO Interface, *ACS Appl. Mater. Interfaces*, 2021, **14**(18), 20368–20374, DOI: **10.1021/acsami.1c15669**.

21 Z. Zhu, X. Li, Y. Qu, F. Zhou, Z. Wang, W. Wang, C. Zhao, H. Wang, L. Li, Y. Yao, Q. Zhang and Y. Wu, A hierarchical heterostructure of CdS QDs confined on 3D $ZnIn_2S_4$ with boosted charge transfer for photocatalytic CO_2 reduction, *Nano Res.*, 2021, **14**, 81–90, DOI: **10.1007/s12274-020-3045-9**.

22 S. Wang, B. Y. Guan and X. W. D. Lou, Construction of $ZnIn_2S_4$–In_2O_3 Hierarchical Tubular Heterostructures for Efficient CO_2 Photoreduction, *J. Am. Chem. Soc.*, 2018, **140**, 5037–5040, DOI: **10.1021/jacs.8b02200**.

23 W. Luo, A. Li, B. Yang, H. Pang, J. Fu, G. Chen, M. Liu, X. Liu, R. Ma, J. Ye and N. Zhang, Synthesis of a Hexagonal Phase ZnS Photocatalyst for High CO Selectivity in CO_2 Reduction Reactions, *ACS Appl. Mater. Interfaces*, 2023, **15**, 15387–15395, DOI: **10.1021/acsami.2c21966**.

24 S. Wang, B. Y. Guan, X. Wang and X. W. D. Lou, Formation of Hierarchical Co_9S_8@$ZnIn_2S_4$ Heterostructured Cages as

an Efficient Photocatalyst for Hydrogen Evolution, *J. Am. Chem. Soc.*, 2018, **140**, 15145–15148, DOI: **10.1021/jacs.8b07721**.

25 N. Abid, A. M. Khan, S. Shujait, K. Chaudhary, M. Ikram, M. Imran, J. Haider, M. Khan, Q. Khan and M. Maqbool, Synthesis of nanomaterials using various top-down and bottom-up approaches, influencing factors, advantages, and disadvantages: A review, *Adv. Colloid Interface Sci.*, 2022, **300**, 102597, DOI: **10.1016/j.cis.2021.102597**.

26 Y. Zhao, Y. Chen, Z. Guan, Y. Ding, J. Lin and G. Tian, Efficient charge transfer in cadmium sulfide quantum dot-decorated hierarchical zinc sulfide-coated tin disulfide cages for carbon dioxide photoreduction, *J. Colloid Interface Sci.*, 2022, **615**, 606–616, DOI: **10.1016/j.jcis.2022.01.195**.

27 A. Sabbah, I. Shown, M. Qorbani, F. Y. Fu, T. Y. Lin, H. L. Wu, P. W. Chung, C. I. Wu, S. R. M. Santiago, J. L. Shen, K. H. Chen and L. C. Chen, Boosting photocatalytic CO_2 reduction in a $ZnS/ZnIn_2S_4$ heterostructure through strain-induced direct *Z*-scheme and a mechanistic study of molecular CO_2 interaction thereon, *Nano Energy*, 2022, **93**, 106809, DOI: **10.1016/j.nanoen.2021.106809**.

28 A. Raza, A. A. Haidry and J. Saddique, In-situ synthesis of Cu_2ZnSnS_4/g-C_3N_4 heterojunction for superior visible light-driven CO_2 reduction, *J. Phys. Chem. Solids*, 2022, **165**, 110694, DOI: **10.1016/j.jpcs.2022.110694**.

29 J. Liu, M. Liu, S. Zheng, X. Liu, S. Yao, F. Jing and G. Chen, Interfacial intimacy and internal electric field modulated S-scheme Sv-$ZnS/ZnIn_2S_4$ photocatalyst for efficient H_2 evolution and CO_2 reduction, *J. Colloid Interface Sci.*, 2023, **635**, 284–294, DOI: **10.1016/j.jcis.2022.12.131**.

30 A. Sabbah, I. Shown, M. Qorbani, F. Y. Fu, T. Y. Lin, H. L. Wu, P. W. Chung, C. I. Wu, S. R. M. Santiago, J. L. Shen, K. H. Chen and L. C. Chen, Boosting photocatalytic CO_2 reduction in a $ZnS/ZnIn_2S_4$ heterostructure through strain-induced direct *Z*-scheme and a mechanistic study of molecular CO_2 interaction thereon, *Nano Energy*, 2022, **93**, 106809, DOI: **10.1016/j.nanoen.2021.106809**.

31 J. Du, H. Shi, J. Wu, K. Li, C. Song and X. Guo, Interface and Defect Engineering of a Hollow $TiO_2@ZnIn_2S_4$ Heterojunction for Highly Enhanced CO_2 Photoreduction Activity, ACS Sustain, *Chem. Eng.*, 2023, **11**, 2531–2540, DOI: **10.1021/acssuschemeng.2c06693**.

32 E. Kim, K. H. Do, J. Wang, Y. Hong, A. Putta Rangappa, D. Amaranatha Reddy, D. Praveen Kumar and T. K. Kim, Construction of 1D TiO_2 nanotubes integrated ultrathin 2D $ZnIn_2S_4$ nanosheets heterostructure for highly efficient and selective photocatalytic CO_2 reduction, *Appl. Surf. Sci.*, 2022, **587**, 152895, DOI: **10.1016/j.apsusc.2022.152895**.

33 M. Yu, X. Lv, A. Mahmoud Idris, S. Li, J. Lin, H. Lin, J. Wang and Z. Li, Upconversion nanoparticles coupled with hierarchical $ZnIn_2S_4$ nanorods as a near-infrared responsive photocatalyst for photocatalytic CO_2 reduction, *J. Colloid Interface Sci.*, 2022, **612**, 782–791, DOI: **10.1016/j.jcis.2021.12.197**.

34 K. Zhu, J. Ou-Yang, Q. Zeng, S. Meng, W. Teng, Y. Song, S. Tang and Y. Cui, Fabrication of hierarchical $ZnIn_2S_4@CNO$ nanosheets for photocatalytic hydrogen production and CO_2 photoreduction, *Chin. J. Catal.*, 2020, **41**, 454–463, DOI: **10.1016/S1872-2067(19)63494-7**.

35 A. Raza, A. A. Haidry and J. Saddique, In-situ synthesis of Cu_2ZnSnS_4/g-C_3N_4 heterojunction for superior visible light-driven CO_2 reduction, *J. Phys. Chem. Solids*, 2022, **165**, 110694, DOI: **10.1016/j.jpcs.2022.110694**.

36 A. Raza, H. Shen, A. A. Haidry, M. K. Shahzad and L. Sun, Facile in-situ fabrication of TiO_2–Cu_2ZnSnS_4 hybrid nanocomposites and their photoreduction of CO_2 to CO/CH_4 generation, *Appl. Surf. Sci.*, 2020, **529**, 147005, DOI: **10.1016/j.apsusc.2020.147005**.

37 M. Zubair, A. Razzaq, C. A. Grimes and S. Il In, Cu_2ZnSnS_4 (CZTS)-ZnO: A noble metal-free hybrid *Z*-scheme photocatalyst for enhanced solar-spectrum photocatalytic conversion of CO_2 to CH_4, *J. CO2 Util.*, 2017, **20**, 301–311, DOI: **10.1016/j.jcou.2017.05.021**.

38 J. Gan, H. Wang, H. Hu, M. Su, F. Chen and H. Xu, Efficient synthesis of tunable band-gap CuInZnS decorated g-C_3N_4 hybrids for enhanced CO_2 photocatalytic reduction and near-infrared-triggered photodegradation performance, *Appl. Surf. Sci.*, 2021, **564**, 150396, DOI: **10.1016/j.apsusc.2021.150396**.

39 P. Madhusudan, S. Wageh, A. A. Al-Ghamdi, J. Zhang, B. Cheng and Y. Yu, Graphene-$Zn_{0.5}Cd_{0.5}S$ nanocomposite with enhanced visible-light photocatalytic CO_2 reduction activity, *Appl. Surf. Sci.*, 2020, **506**, 144683, DOI: **10.1016/j.apsusc.2019.144683**.

40 Y. Su, Z. Zhang, H. Liu and Y. Wang, $Cd_{0.2}Zn_{0.8}S@UiO$-66-NH_2 nanocomposites as efficient and stable visible-light-driven photocatalyst for H_2 evolution and CO_2 reduction, *Appl. Catal., B*, 2017, **200**, 448–457, DOI: **10.1016/j.apcatb.2016.07.032**.

41 A. Saeed, W. Chen, A. H. Shah, Y. Zhang, I. Mehmood and Y. Liu, Enhancement of photocatalytic CO_2 reduction for novel $Cd_{0.2}Zn_{0.8}S@Ti_3C_2$(MXenes) nanocomposites, *J. CO2 Util.*, 2021, **47**, 101501, DOI: **10.1016/j.jcou.2021.101501**.

42 X. Zhang, D. Kim and L. Y. S. Lee, Copper-Doped ZnS with Internal Phase Junctions for Highly Selective CO Production from CO_2 Photoreduction, *ACS Appl. Energy Mater.*, 2021, **4**, 2586–2592, DOI: **10.1021/acsaem.0c03163**.

43 J. Chen, F. Xin, S. Qin and X. Yin, Photocatalytically reducing CO_2 to methyl formate in methanol over ZnS and Ni-doped ZnS photocatalysts, *Chem. Eng. J.*, 2013, **230**, 506–512, DOI: **10.1016/j.cej.2013.06.119**.

44 H. Il Nam, K. Ryeol Park, Y. W. Choi, H. Ji Sim, K. Yong Sohn and D. H. Lim, Electrocatalytic CO_2 reduction using self-supported zinc sulfide arrays for selective CO production, *Appl. Surf. Sci.*, 2023, **612**, 155646, DOI: **10.1016/j.apsusc.2022.155646**.

45 N. Pokhrel, P. K. Vabbina and N. Pala, Sonochemistry: Science and Engineering, *Ultrason. Sonochem.*, 2016, **29**, 104–128, DOI: **10.1016/j.ultsonch.2015.07.023**.

46 M. Hujjatul Islam, M. T. Y. Paul, O. S. Burheim and B. G. Pollet, Recent developments in the sonoelectrochemical

synthesis of nanomaterials, *Ultrason. Sonochem.*, 2019, **59**, 104711, DOI: **10.1016/j.ultsonch.2019.104711**.

47 H. L. Zhu, L. C. Liu, Z. Y. Li, J. J. Ma, Y. Q. Zheng and M. Shui, Insight into the Active Site in Electrochemical CO_2 Reduction of Self-Supported Cobalt Phthalocyanine Anchored on $ZnIn_2S_4$ Nanoarrays, *ACS Appl. Energy Mater.*, 2021, **4**, 6616–6623, DOI: **10.1021/acsaem.1c00672**.

48 M. Baniamer, A. Aroujalian and S. Sharifnia, A novel PEBAX-1657/PES-($BiFeO_3$@ZnS) photocatalytic membrane for integrated hybrid systems coupling CO_2 separation and photoreduction, *J. Environ. Chem. Eng.*, 2021, **9**, 106529, DOI: **10.1016/j.jece.2021.106529**.

49 J. Chen, F. Xin, X. Yin, T. Xiang and Y. Wang, Synthesis of hexagonal and cubic $ZnIn_2S_4$ nanosheets for the photo-catalytic reduction of CO_2 with methanol, *RSC Adv.*, 2015, **5**, 3833–3839, DOI: **10.1039/c4ra13191f**.

50 H. K. Lin, T. Yan, S. Bashir and J. L. Liu, Chapter 3 - Synthesis of nanomaterials using bottom-up methods, *Advanced Nanomaterials and Their Applications in Renewable Energy*, Elsevier Inc., 2nd edn, 2022, pp. 61–110, DOI: **10.1016/B978-0-323-99877-2.00003-5**.

51 T. Baran, S. Wojtyła, A. Dibenedetto, M. Aresta and W. Macyk, Zinc sulfide functionalized with ruthenium nanoparticles for photocatalytic reduction of CO_2, *Appl. Catal., B*, 2015, **178**, 170–176, DOI: **10.1016/j.apcatb.2014.09.052**.

52 H. Pang, X. Meng, H. Song, W. Zhou, G. Yang, H. Zhang, Y. Izumi, T. Takei, W. Jewasuwan, N. Fukata and J. Ye, Probing the role of nickle dopant in aqueous colloidal ZnS nanocrystals for efficient solar-driven Nickel reduction, *Appl. Catal., B*, 2019, **244**, 1013–1020, DOI: **10.1016/j.apcatb.2018.12.010**.

53 T. M. Suzuki, T. Takayama, S. Sato, A. Iwase, A. Kudo and T. Morikawa, Enhancement of CO_2 reduction activity under visible light irradiation over Zn-based metal sulfides by combination with Ru-complex catalysts, *Appl. Catal., B*, 2018, **224**, 572–578, DOI: **10.1016/j.apcatb.2017.10.053**.

54 A. Li, H. Pang, P. Li, N. Zhang, G. Chen, X. Meng, M. Liu, X. Liu, R. Ma and J. Ye, Insights into the critical dual-effect of acid treatment on $Zn_xCd_{1−x}S$ for enhanced photocata-lytic production of syngas under visible light, *Appl. Catal., B*, 2021, **288**, 1–10, DOI: **10.1016/j.apcatb.2021.119976**.

55 L. Cheng, D. Zhang, Y. Liao, J. Fan and Q. Xiang, Structural engineering of 3D hierarchical $Cd_{0.8}Zn_{0.2}S$ for selective photocatalytic CO_2 reduction, *Chin. J. Catal.*, 2020, **42**, 131–140, DOI: **10.1016/S1872-2067(20)63623-3**.

56 D. Jiang, Q. Zhang, D. Chen, B. Wen, Q. Song, C. Zhou and D. Li, $KCa_2Nb_3O_{10}$/$ZnIn_2S_4$ nanosheet heterojunctions with improved charge separation efficiency for efficient photocatalytic CO_2 reduction, *J. Alloys Compd.*, 2021, **865**, 158836, DOI: **10.1016/j.jallcom.2021.158836**.

57 A. Kajbafvala, H. Bahmanpour, M. H. Maneshian and M. Li, Self-Assembly Techniques for Nanofabrication, *J. Nanomater.*, 2013, **2013**, 158517, DOI: **10.1155/2013/158517**.

58 P. Madhusudan, R. Shi, S. Xiang, M. Jin, B. N. Chandrashekar, J. Wang, W. Wang, O. Peng, A. Amini and C. Cheng, Construction of highly efficient *Z*-scheme $Zn_xCd_{1−x}S$/Au@g-C_3N_4 ternary heterojunction composite for visible-light-driven photocatalytic reduction of CO_2 to solar fuel, *Appl. Catal., B*, 2021, **282**, 119600, DOI: **10.1016/j.apcatb.2020.119600**.

59 Y. Y. Ren, W. Xia, B. Y. Deng, J. Liu and F. Wang, Host-guest assemblies of anchoring molecular catalysts of CO_2 reduction onto $CuInS_2$/ZnS quantum dots for robust photocatalytic syngas production in water, *Mol. Catal.*, 2022, **520**, 112168, DOI: **10.1016/j.mcat.2022.112168**.

60 J. Zhao, Q. Huang, Z. Xie, Y. Liu, F. Liu, F. Wei, S. Wang, Z. Zhang, R. Yuan, K. Wu, Z. Ding and J. Long, Hierarchical Hollow-TiO_2@CdS/ZnS Hybrid for Solar-Driven CO_2-Selective Conversion, *ACS Appl. Mater. Interfaces*, 2023, **15**, 24494–24503, DOI: **10.1021/acsami.3c03255**.

61 J. Van Embden, A. S. R. Chesman and J. J. Jasieniak, The heat-up synthesis of colloidal nanocrystals, *Chem. Mater.*, 2015, **27**, 2246–2285, DOI: **10.1021/cm5028964**.

62 M. Niederberger and G. Garnweitner, Organic reaction pathways in the nonaqueous synthesis of metal oxide nanoparticles, *Chem. – Eur. J.*, 2006, **12**, 7282–7302, DOI: **10.1002/chem.200600313**.

63 G. Singh, V. S. Myasnichenko and W. R. Glomm, New insights into size-controlled reproducible synthesis of ani-sotropic Fe_3O_4 nanoparticles: The importance of the reac-tion environment, *Mater. Adv.*, 2020, **1**, 1077–1082, DOI: **10.1039/d0ma00275e**.

64 A. T. Odularu, Metal Nanoparticles: Thermal Decomposi-tion, Biomedicinal Applications to Cancer Treatment, and Future Perspectives, *Bioinorg. Chem. Appl.*, 2018, **2018**, 9354708, DOI: **10.1155/2018/9354708**.

65 F. Tang, L. Wang, L. Ma, Y. Fang, J. Huang and Y. N. Liu, Protein-Zn(ɪɪ) networks derived N-doped porous carbon-supported ZnS for photothermally catalytic CO_2 conver-sion, *J. CO2 Util.*, 2021, **45**, 101431, DOI: **10.1016/j.jcou.2020.101431**.

66 S. Yoshino, A. Iwase, Y. Yamaguchi, T. M. Suzuki, T. Morikawa and A. Kudo, Photocatalytic CO_2 Reduction Using Water as an Electron Donor under Visible Light Irradiation by *Z*-Scheme and Photoelectrochemical Sys-tems over $(CuGa)_{0.5}ZnS_2$ in the Presence of Basic Additives, *J. Am. Chem. Soc.*, 2022, **144**, 2323–2332, DOI: **10.1021/jacs.1c12636**.

67 R. M. Mohamed, I. A. Mkhalid, M. Alhaddad, A. Basaleh, K. A. Alzahrani and A. A. Ismail, Construction of hierarchical ZnS@ZnO secured from metal–organic framework-ZnS@ZIF-8 for enhanced photoreduction of CO_2, *J. Taiwan Inst. Chem. Eng.*, 2021, **127**, 208–219, DOI: **10.1016/j.jtice.2021.08.017**.

68 N.-T. Nguyen, Fabrication technologies, *Micro and Nano Tech-nologies*, Micromixers (Second Edition) Fundamentals, Design and Fabrication, 2012, pp. 113–161, DOI: **10.1016/b978-1-4377-3520-8.00004-8**.

69 B. S. Yilbas, A. Al-Sharafi and H. Ali, *Surfaces for Self-Cleaning*, 2019, DOI: **10.1016/b978-0-12-814776-4.00003-3**.

70 T. Yoshida, A. Yamaguchi, N. Umezawa and M. Miyauchi, Photocatalytic CO_2 Reduction Using a Pristine Cu_2ZnSnS_4

Film Electrode under Visible Light Irradiation, *J. Phys. Chem. C*, 2018, **122**, 21695–21702, DOI: **10.1021/acs.jpcc.8b04241**.

71 H. Tuan Nguyen, A. Tuan Duong and S. Lee, Fabrication and enhanced performance of LEDs based on multilayer CdSe@ZnS quantum dot films using layer-by-layer spin-coating with solid-state treatment, *Chem. Phys.*, 2023, **572**, 111954, DOI: **10.1016/j.chemphys.2023.111954**.

72 N. Kumar, L. P. Purohit and Y. C. Goswami, Spin coating of ZnS nanostructures on filter paper and their characterization, *Phys. E*, 2016, **83**, 333–338, DOI: **10.1016/j.physe.2016.04.025**.

73 C. Li, G. Shen, R. Zhang, D. Wu, C. Zou, T. Ling, H. Liu, C. Dong and X.-W. Du, Zn nanosheets coated with a ZnS subnanometer layer for effective and durable CO_2 reduction, *J. Mater. Chem. A*, 2019, **7**, 1418–1423.

74 J.-Z. Zhen, J.-X. Liu, T.-Y. Chen, F. Shi, Y.-N. Dai, B. Yang, Y.-F. Li, X. Wang, T.-G. Nong and Y.-Q. Hu, Fabrication of ZnS/Zn electrode using sulphur infiltration method for CO_2 reduction into CO in organic media, *J. Alloys Compd.*, 2019, **771**, 994–999.

75 J.-Z. Zhen, J.-X. Liu, T.-Y. Chen, F. Shi, Y.-N. Dai, B. Yang, Y.-F. Li, X. Wang, T.-G. Nong, Y.-Q. Hu and J. Shi, Fabrication of ZnS/Zn electrode using sulphur infiltration method for CO_2 reduction into CO in organic media, *J. Alloys Compd.*, 2019, **771**, 994–999, DOI: **10.1016/j.jallcom.2018.08.318**.

76 K. Kočí, M. Reli, O. Kozák, Z. Lacný, D. Plachá, P. Praus and L. Obalová, Influence of reactor geometry on the yield of CO_2 photocatalytic reduction, *Catal. Today*, 2011, **176**, 212–214.

77 F. Tang, L. Wang, L. Ma, Y. Fang, J. Huang and Y.-N. Liu, Protein-Zn(II) networks derived N-doped porous carbon-supported ZnS for photothermally catalytic CO_2 conversion, *J. CO2 Util.*, 2021, **45**, 101431.

78 U. Mustapha, C. C. Nnadiekwe, M. A. Alhaboudal, U. Yunusa, A. H. S. Abdullahi, I. Abdulazeez, I. Hussain, S. A. Ganiyu, A. A. Al-Saadi and K. Alhooshani, The role of morphology on the electrochemical CO_2 reduction performance of transition metal-based catalysts, *J. Energy Chem.*, 2023, **85**, 198–219, DOI: **10.1016/j.jechem.2023.06.010**.

79 E. P. Komarala, A. A. Alkhoori, X. Zhang, H. M. Cheng and K. Polychronopoulou, Design and synthesis of thermally stable single atom catalysts for thermochemical CO_2 reduction, *J. Energy Chem.*, 2023, **86**, 246–262, DOI: **10.1016/j.jechem.2023.07.032**.

80 H. Pang, F. Ichihara, X. Meng, L. Li, Y. Xiao, W. Zhou and J. Ye, Selectivity control of photocatalytic CO_2 reduction over ZnS-based nanocrystals: A comparison study on the role of ionic cocatalysts, *J. Energy Chem.*, 2023, **86**, 391–398, DOI: **10.1016/j.jechem.2023.07.031**.

81 P. Li, G. Luo, S. Zhu, L. Guo, P. Qu and T. He, Unraveling the selectivity puzzle of H_2 evolution over CO_2 photoreduction using ZnS nanocatalysts with phase junction, *Appl. Catal., B*, 2020, **274**, 119115, DOI: **10.1016/j.apcatb.2020.119115**.

82 R. Zhou and M. I. Guzman, CO_2 reduction under periodic illumination of ZnS, *J. Phys. Chem. C*, 2014, **118**, 11649–11656.

83 J. Fu, J. Yu, C. Jiang and B. Cheng, g-C_3N_4-Based Heterostructured Photocatalysts, *Adv. Energy Mater.*, 2017, **8**, 1–31, DOI: **10.1002/aenm.201701503**.

84 U. M. Shahed Khan, M. Frites, Y. A. Shaban and M. M. Grey, Photocatalytic and Photoelectrochemical Reduction of CO_2 to Methanol in Aqueous Medium, *J. Chem. Appl.*, 2019, **5**, 12.

85 J. Bian, Z. Zhang, Y. Liu, E. Chen, J. Tang and L. Jing, Strategies and reaction systems for solar-driven CO_2 reduction by water, *Neutrality*, 2022, 1–20.

86 M. Aresta, A. Dibenedetto and E. Quaranta, *Reaction Mechanisms in Carbon Dioxide Conversion*, Springer-Verlag, Berlin, 2016.

87 X. Chen, C. Zhao, H. Wu, Y. Shi, C. Chen and X. Zhou, Z-Scheme Photocatalyst for Overall Water Splitting: A DFT Study, *Materials*, 2022, **15**, 3786.

88 J. Low, J. Yu, M. Jaroniec, S. Wageh and A. A. Al-Ghamdi, Heterojunction Photocatalysts, *Adv. Mater.*, 2017, **29**, 1–20, DOI: **10.1002/adma.201601694**.

89 T. Jin, C. Liu, F. Chen, J. Qian, Y. Qiu, X. Meng and Z. Chen, Synthesis of g-C_3N_4/CQDs composite and its photocatalytic degradation property for Rhodamine B, *Carbon Lett.*, 2022, **32**, 1451–1462, DOI: **10.1007/s42823-022-00382-2**.

90 X. Xu, S. Li, J. Chen, S. Cai, Z. Long and X. Fang, Design Principles and Material Engineering of ZnS for Optoelectronic Devices and Catalysis, *Adv. Funct. Mater.*, 2018, **28**, 1–24, DOI: **10.1002/adfm.201802029**.

91 M. Sheraz, L. Shi, B. Zou and H. Ullah, Optik Eff ect of Vanadium doping on optoelectronic and magnetic properties of wurtzite ZnS crystal, *Optik*, 2020, **204**, 164162, DOI: **10.1016/j.ijleo.2019.164162**.

92 Y. Hanifehpour, B. Soltani, A. R. Amani-Ghadim, B. Hedayati, B. Khomami and S. W. Joo, Praseodymium-doped ZnS nanomaterials: Hydrothermal synthesis and characterization with enhanced visible light photocatalytic activity, *J. Ind. Eng. Chem.*, 2016, **34**, 41–50, DOI: **10.1016/j.jiec.2015.10.032**.

93 J. Low, J. Yu and C. Jiang, Design and fabrication of direct Z-scheme photocatalysts, *Interface Sci. Technol.*, 2020, **31**, 193–229, DOI: **10.1016/B978-0-08-102890-2.00006-3**.

94 P. Bakhtkhosh and A. Mehrizad, Sonochemical synthesis of Sm-doped ZnS nanoparticles for photocatalytic degradation of Direct Blue 14: Experimental design by response surface methodology and development of a kinetics model, *J. Mol. Liq.*, 2017, **240**, 65–73, DOI: **10.1016/j.molliq.2017.05.053**.

95 M. Jothibas, C. Manoharan, S. Johnson Jeyakumar, P. Praveen, I. Kartharinal Punithavathy and J. Prince Richard, Synthesis and enhanced photocatalytic property of Ni doped ZnS nanoparticles, *Sol. Energy*, 2018, **159**, 434–443, DOI: **10.1016/j.solener.2017.10.055**.

96 L. Wang, P. Wang, B. Huang, X. Ma, G. Wang, Y. Dai, X. Zhang and X. Qin, Synthesis of Mn-doped ZnS microspheres with enhanced visible light photocatalytic activity, *Appl. Surf. Sci.*, 2017, **391**, 557–564, DOI: **10.1016/j.apsusc.2016.06.159**.

97 J. Zhou, J. Zhao and R. Liu, Defect engineering of zeolite imidazole framework derived ZnS nanosheets towards enhanced visible light driven photocatalytic hydrogen production, *Appl. Catal., B*, 2020, **278**, 119265, DOI: **10.1016/j.apcatb.2020.119265**.

98 Z. Fang, S. Weng, X. Ye, W. Feng, Z. Zheng, M. Lu, S. Lin, X. Fu and P. Liu, Defect Engineering and Phase Junction Architecture of Wide-Bandgap ZnS for Conflicting Visible Light Activity in Photocatalytic H$_2$ Evolution, *ACS Appl. Mater. Interfaces*, 2015, 7, 13915–13924, DOI: **10.1021/acsami.5b02641**.

99 E. B. Yazdani and A. Mehrizad, Sonochemical preparation and photocatalytic application of Ag-ZnS-MWCNTs composite for the degradation of Rhodamine B under visible light: Experimental design and kinetics modeling, *J. Mol. Liq.*, 2018, **255**, 102–112, DOI: **10.1016/j.molliq.2018.01.154**.

100 O. Sacco, V. Vaiano, D. Sannino, R. A. Picca and N. Cioffi, Ag modified ZnS for photocatalytic water pollutants degradation: Influence of metal loading and preparation method, *J. Colloid Interface Sci.*, 2019, **537**, 671–681, DOI: **10.1016/j.jcis.2018.11.073**.

101 G. Di Liberto, S. Tosoni and G. Pacchioni, Charge Carriers Cascade in a Ternary TiO$_2$/TiO$_2$/ZnS Heterojunction: A DFT Study, *ChemCatChem*, 2020, **12**, 2097–2105, DOI: **10.1002/cctc.201902351**.

102 Y. Che, B. Lu, Q. Qi, H. Chang, J. Zhai, K. Wang and Z. Liu, Bio-inspired *Z*-scheme g-C$_3$N$_4$/Ag$_2$CrO$_4$ for efficient visible-light photocatalytic hydrogen generation, *Sci. Rep.*, 2018, **8**, 1–12, DOI: **10.1038/s41598-018-34287-w**.

103 G. Wang, S. Lv, Y. Shen, W. Li, L. Lin and Z. Li, Advancements in heterojunction, cocatalyst, defect and morphology engineering of semiconductor oxide photocatalysts, *J. Mater.*, 2023, 2352–8478, DOI: **10.1016/j.jmat.2023.05.014**.

104 J. Murillo-Sierra, A. Hernández-Ramírez, D. A. Pino-Sandoval, E. Ruiz-Ruiz and A. Martínez-Hernández, Promoting multielectron CO$_2$ reduction using a direct *Z*-scheme WO$_3$/ZnS photocatalyst, *J. CO2 Util.*, 2022, **63**, 102122, DOI: **10.1016/j.jcou.2022.102122**.

105 Y. Xu, H. Yan and T. Chen, Application of ZnO/WO$_3$ Composite Nanofiber Photocatalysts in Textile Wastewater Treatment, *Separations*, 2023, **10**, 339.

106 X. Zhu, D. Wang and S. Hui, Review Article Research Progress of Adsorption and Photocatalysis of Formaldehyde on TiO$_2$/AC, *Adsorpt. Sci. Technol.*, 2021, **2021**, 1–16.

107 J. C. Murillo-sierra, A. Hern and A. Martínez-hern, Journal of Environmental Chemical Engineering Construction of direct *Z*-scheme WO$_3$/ZnS heterojunction to enhance the photocatalytic degradation of tetracycline antibiotic, *J. Environ. Chem. Eng.*, 2021, **9**, 105111, DOI: **10.1016/j.jece.2021.105111**.

108 S. Hussain, Y. Wang, L. Guo and T. He, Theoretical insights into the mechanism of photocatalytic reduction of CO$_2$ over semiconductor catalysts, *J. Photochem. Photobiol., C*, 2022, **52**, 100538, DOI: **10.1016/j.jphotochemrev.2022.100538**.

109 A. Kidanemariam, J. Lee and J. Park, Recent Innovation of Metal-Organic Frameworks for Carbon Dioxide Photocatalytic Reduction, *Polymers*, 2019, **11**, 2090.

110 A. Razzaq and S. In, TiO$_2$ Based Nanostructures for Photocatalytic CO 2 Conversion to Valuable Chemicals, *Micromachines*, 2019, **10**, 326.

111 J. Wu, Y. Huang, W. Ye and Y. Li, CO$_2$ Reduction: From the Electrochemical to Photochemical Approach, *Adv. Sci.*, 2017, **4**, 1700194, DOI: **10.1002/advs.201700194**.

112 R. Zhou and M. I. Guzman, CO$_2$ Reduction under Periodic Illumination of ZnS, *J. Phys. Chem. C*, 2014, **118**, 11649–11656.

113 K. Muldoon, Y. Song, Z. Ahmad, X. Chen and M. W. Chang, High Precision 3D Printing for Micro to Nano Scale Biomedical and Electronic Devices, *Micromachines*, 2022, **13**(4), 642, DOI: **10.3390/mi13040642**.

114 X. Hao, Z. Cui, J. Zhou, Y. Hu, Y. Wang and Z. Zou, Author's Accepted Manuscript Architecture of high efficient zinc vacancy organic frameworks To appear, *Nano Energy*, 2018, **52**, 105–116, DOI: **10.1016/j.nanoen.2018.07.043**.

115 J. Zhou, Q. Jia, L. Gong, S. Zhang, X. Zhou and H. Song, Enhanced *Z*-scheme ZnS/NH$_2$ − MIL-125 (Ti) photocatalysts with biomass-derived carbon quantum dots for CO$_2$ reduction, *Mol. Catal.*, 2024, **552**, 113715, DOI: **10.1016/j.mcat.2023.113715**.

116 S. Yoshino, A. Iwase, Y. Yamaguchi, T. M. Suzuki, T. Morikawa and A. Kudo, Photocatalytic CO$_2$ Reduction Using Water as an Electron Donor under Visible Light Irradiation by *Z*-Scheme and Photoelectrochemical Systems over (CuGa)$_{0.5}$ZnS$_2$ in the Presence of Basic Additives, *J. Am. Chem. Soc.*, 2022, **144**, 2323–2332, DOI: **10.1021/jacs.1c12636**.

117 H. Park, N. Son, B. Hyun, C. Liu, S. Woo and M. Kang, Switching of a type I to an all-solid-state *Z*-scheme heterojunction by an electron mediator rGO bridge: 18. 4% solar-to-hydrogen efficiency in n-ZnS/rGO/p-Bi$_2$S$_3$ ternary catalyst, *Chem. Eng. J.*, 2022, **430**, 133104, DOI: **10.1016/j.cej.2021.133104**.

118 P. Li and T. He, Common-cation based *Z*-scheme ZnS@ZnO core-shell nanostructure for efficient solar-fuel production, *Appl. Catal., B*, 2018, **238**, 518–524, DOI: **10.1016/j.apcatb.2018.07.057**.

119 C. Yang, J. Wang, R. Wang, W. Zhu, L. Zhang, T. Du, J. Sun, M.-Q. Zhu, Y. Shen and J. Wang, Efficient hollow cubic Co$_9$S$_8$@defective ZnS/g-C$_3$N$_4$ for multi-pollutants removal *via* cascade *Z*-scheme heterojunction, *Appl. Catal., B*, 2023, **322**, 122084, DOI: **10.1016/j.apcatb.2022.122084**.

120 J. Fu, Q. Xu, J. Low, C. Jiang and J. Yu, Ultrathin 2D/2D WO$_3$/g-C$_3$N$_4$ step-scheme H$_2$-production photocatalyst, *Appl. Catal., B*, 2019, **243**, 556–565, DOI: **10.1016/j.apcatb.2018.11.011**.

121 Y. Bao, S. Song, G. Yao and S. Jiang, S-Scheme Photocatalytic Systems, *Sol. RRL*, 2021, **2100118**, 1–13, DOI: **10.1002/solr.202100118**.

122 Z. Zhu, Z. Lu, T. Xu, C. Chen, G. Yang, T. Zha, J. Lu and Y. Xue, Arbidol monotherapy is superior to lopinavir/ritonavir in treating COVID-19, *J. Infect.*, 2020, 19–21, DOI: **10.1016/j.jinf.2020.03.060**.

123 Z. Liu, J. Xu, C. Xiang, Y. Liu, L. Ma and L. Hu, S-scheme heterojunction based on ZnS/CoMoO$_4$ ball-and-rod

composite photocatalyst to promote photocatalytic hydrogen production, *Appl. Surf. Sci.*, 2021, **569**, 150973, DOI: **10.1016/j.apsusc.2021.150973**.

124 R. M. Mohamed, I. A. Mkhalid, M. Alhaddad, A. Basaleh, K. A. Alzahrani and A. A. Ismail, Enhanced CO_2 photocatalytic conversion into CH_3OH over visible-light-driven Pt nanoparticle-decorated mesoporous ZnO–ZnS S-scheme heterostructures, *Ceram. Int.*, 2021, **47**, 26779–26788, DOI: **10.1016/j.ceramint.2021.06.086**.

125 J. Liu, M. Liu, S. Zheng, X. Liu, S. Yao, F. Jing and G. Chen, Interfacial intimacy and internal electric field modulated S-scheme Sv-ZnS/ZnIn$_2$S$_4$ photocatalyst for efficient H_2 evolution and CO_2 reduction, *J. Colloid Interface Sci.*, 2023, **635**, 284–294, DOI: **10.1016/j.jcis.2022.12.131**.

126 L. Li, D. Ma, Q. Xu and S. Huang, Constructing hierarchical ZnIn$_2$S$_4$/g-C$_3$N$_4$ S-scheme heterojunction for boosted CO_2 photoreduction performance, *Chem. Eng. J.*, 2022, **437**, 135153, DOI: **10.1016/j.cej.2022.135153**.

127 Y. Zhang, M. Xu, W. Zhou, X. Song, X. Liu, J. Zhang, S. Chen and P. Huo, Fabricated ZnO@ZnIn$_2$S$_4$ S-scheme heterojunction photocatalyst for enhanced electron-transfer and CO_2 reduction, *J. Colloid Interface Sci.*, 2023, **650**, 1762–1772, DOI: **10.1016/j.jcis.2023.07.120**.

128 M. U. Shahid, T. Najam, M. H. Helal, I. Hossain, S. M. El-Bahy, Z. M. El-Bahy, A. ur Rehman, S. S. A. Shah and M. A. Nazir, Transition metal chalcogenides and phosphides for photocatalytic H_2 generation *via* water splitting: a critical review, *Int. J. Hydrogen Energy*, 2024, **62**, 1113–1138.

129 S. Chandrasekaran, L. Yao, L. Deng, C. Bowen, Y. Zhang, S. Chen, Z. Lin, F. Peng and P. Zhang, Recent advances in metal sulfides: from controlled fabrication to electrocatalytic, photocatalytic and photoelectrochemical water splitting and beyond, *Chem. Soc. Rev.*, 2019, **48**, 4178–4280.

130 Y. Meng, G. Liu, G. Zuo, X. Meng, T. Wang and J. Ye, A review on ZnS-based photocatalysts for CO_2 reduction in all-inorganic aqueous medium, *Nanoscale*, 2022, **14**, 14455–14465, DOI: **10.1039/d2nr03703c**.

131 P. Weide, K. Schulz, S. Kaluza, M. Rohe, R. Beranek and M. Muhler, Controlling the Photocorrosion of Zinc Sulfide Nanoparticles in Water by Doping with Chloride and Cobalt Ions, *Langmuir*, 2016, **32**, 12641–12649, DOI: **10.1021/acs.langmuir.6b03385**.

132 M. Dimitropoulos, C. A. Aggelopoulos, L. Sygellou, S. T. Tsantis, P. G. Koutsoukos and S. N. Yannopoulos, Unveiling the photocorrosion mechanism of zinc oxide photocatalyst: Interplay between surface corrosion and regeneration, *J. Environ. Chem. Eng.*, 2024, **12**, 112102, DOI: **10.1016/j.jece.2024.112102**.

133 M. J. Nine, M. A. Cole, D. N. H. Tran and D. Losic, Graphene: a multipurpose material for protective coatings, *J. Mater. Chem. A*, 2015, **3**, 12580–12602.

134 T. Lange, S. Reichenberger, S. Ristig, M. Rohe, J. Strunk, S. Barcikowski and R. Schlögl, Zinc sulfide for photocatalysis: White angel or black sheep?, *Prog. Mater. Sci.*, 2022, **124**, 100865.

135 S. Kumar, A. Kumar, V. Navakoteswara Rao, A. Kumar, M. V. Shankar and V. Krishnan, Defect-rich MoS$_2$ ultrathin nanosheets-coated nitrogen-doped ZnO nanorod heterostructures: an insight into in-situ-generated ZnS for enhanced photocatalytic hydrogen evolution, *ACS Appl. Energy Mater.*, 2019, **2**, 5622–5634.

136 L. Bao, S. Ali, C. Dai, Q. Zeng, C. Zeng, Y. Jia, X. Liu, P. Wang, X. Ren and T. Yang, A Full-Spectrum ZnS Photocatalyst with Gradient Distribution of Atomic Copper Dopants and Concomitant Sulfur Vacancies for Highly Efficient Hydrogen Evolution, *ACS Nano*, 2024, **18**(7), 5878–5889, DOI: **10.1021/acsnano.3c12773**.

137 B. Zhu, B. Cheng, L. Zhang and J. Yu, Review on DFT calculation of *s*-triazine – based carbon nitride, *Carbon Energy*, 2019, **1**, 32–56, DOI: **10.1002/cey2.1**.

138 W. M. C. Sameera, S. Maeda and K. Morokuma, Computational Catalysis Using the Artificial Force Induced Reaction Method, *Acc. Chem. Res.*, 2016, **49**, 763–773, DOI: **10.1021/acs.accounts.6b00023**.

139 A. R. Zeng, K. Lian, B. Su, L. Lu, J. Lin, D. Tang, S. Lin, X. Wang, R. Zeng, K. Lian, B. Su, L. Lu, J. Lin, D. Tang and S. Lin, Versatile Synthesis of Hollow Metal Sulfides *via* Reverse Cation Exchange Reactions for Photocatalytic CO_2 Reduction, *Angew. Chem., Int. Ed.*, 2021, **60**, 25055–25062, DOI: **10.1002/anie.202110670**.

140 Y. Cheng, J. Chen, P. Wang, W. Liu, H. Che, X. Gao, B. Liu and Y. Ao, Interfacial engineering boosting the piezocatalytic performance of *Z*-scheme heterojunction for carbamazepine degradation: Mechanism, degradation pathway and DFT calculation, *Appl. Catal., B*, 2022, **317**, 121793, DOI: **10.1016/j.apcatb.2022.121793**.

141 P. Malik, R. Thareja, J. Singh and R. Kakkar, II-VI core/shell quantum dots and doping with transition metal ions as a means of tuning the magnetoelectronic properties of CdS/ZnS core/shell QDs: A DFT study, *J. Mol. Graphics Modell.*, 2022, **111**, 108099, DOI: **10.1016/j.jmgm.2021.108099**.

142 L. Oppong-Antwi and J. N. Hart, in *DFT Study of CuS–ZnS Heterostructures BT – Energy Technology 2023*, ed. S. Alam, D. P. Guillen, F. Tesfaye, L. Zhang, S. A. C. Hockaday, N. R. Neelameggham, H. Peng, N. Haque and Y. Liu, Springer Nature, Switzerland, Cham, 2023, pp. 39–50.

143 L. Yan, J. Tang, Q. Qiao, Y. Wang, H. Cai, J. Jin, H. Gao and Y. Xu, Synthesize, construction and enhanced performance of Bi$_2$WO$_6$/ZnS heterojunction under visible light: Experimental and DFT study, *Arabian J. Chem.*, 2023, **16**, 104760, DOI: **10.1016/j.arabjc.2023.104760**.

144 M. F. A. Messih, Expression of Concern: The controlled synthesis and DFT investigation of novel (0D)–(3D) ZnS/SiO$_2$ heterostructures for photocatalytic applications, *RSC Adv.*, 2021, 22352–22364, DOI: **10.1039/d1ra02284a**.

145 M. Dong, P. Zhou, C. Jiang, B. Cheng and J. Yu, First-principles investigation of Cu-doped ZnS with enhanced photocatalytic hydrogen production activity State Key Laboratory of Advanced Technology for Materials

Synthesis, *Chem. Phys. Lett.*, 2016, **668**, 1–6, DOI: **10.1016/j.cplett.2016.12.008**.

146 S. Hussain, L. Guo and T. He, Influence of Vacancy Defects on the Interfacial Structural and Optoelectronic Properties of ZnO/ZnS Heterostructures for Photocatalysis, *Catalysts*, 2023, **13**, 1199.

147 S. Khan, H. Choi, D. Kim and S. Y. Lee, Self-assembled heterojunction of metal sulfides for improved photocatalysis, *Chem. Eng. J.*, 2020, **395**, 125092, DOI: **10.1016/j.cej.2020.125092**.

148 W. Han, F. A. N. Sheng, W. Sen, D. Mei, Z. Qin, W. Fan and J. Wang, Research progresses in the hydrogenation of carbon dioxide to certain hydrocarbon products, *J. Fuel Chem. Technol.*, 2021, **49**, 1609–1619.

149 X. Ma, D. Li, J. Xie, J. Qi, H. Jin, L. Bai, H. Zhang, F. You and F. Yuan, Confined space and heterojunction dual modulation of ZnO/ZnS for boosting photocatalytic CO_2 reduction, *Sol. RRL*, 2023, **7**, 2201093.

150 X. Xu, K. Xie, J. Hu, S. Liu, H. Zhong and H.-R. Wen, The metal-organic frameworks as unique platform for photocatalytic CO_2 conversion to liquid fuels, *J. Environ. Chem. Eng.*, 2023, 110424.

151 T. Mahvelati-Shamsabadi, E. K. Goharshadi, M. Shafaee and Z. Niazi, ZnS@ reduced graphene oxide nanocomposite as an effective sunlight driven photocatalyst for degradation of reactive black 5: a mechanistic approach, *Sep. Purif. Technol.*, 2018, **202**, 326–334.

152 P. Li and T. He, Recent advances in zinc chalcogenide-based nanocatalysts for photocatalytic reduction of CO_2, *J. Mater. Chem. A*, 2021, **9**, 23364–23381.

153 D. Adekoya, M. Tahir and N. A. S. Amin, Recent trends in photocatalytic materials for reduction of carbon dioxide to methanol, *Renewable Sustainable Energy Rev.*, 2019, **116**, 109389.

154 I. Amghizar, L. A. Vandewalle, K. M. Van Geem and G. B. Marin, New trends in olefin production, *Engineering*, 2017, **3**, 171–178.

155 A. Hwang and A. Bhan, Deactivation of zeolites and zeotypes in methanol-to-hydrocarbons catalysis: Mechanisms and circumvention, *Acc. Chem. Res.*, 2019, **52**, 2647–2656.

156 A. Bahuguna and Y. Sasson, Formate-Bicarbonate Cycle as a Vehicle for Hydrogen and Energy Storage, *ChemSusChem*, 2021, **14**, 1258–1283.

157 G. Centi and S. Perathoner, Opportunities and prospects in the chemical recycling of carbon dioxide to fuels, *Catal. Today*, 2009, **148**, 191–205.

158 E. Alper and O. Y. Orhan, CO_2 utilization: Developments in conversion processes, *Petroleum*, 2017, **3**, 109–126.

159 B. C. Dharmalingam, A. Koushik V, M. Mureddu, L. Atzori, S. Lai, A. Pettinau, N. S. Kaisare, P. Aghalayam and J. J. Varghese, Unravelling the role of metal-metal oxide interfaces of $Cu/ZnO/ZrO_2/Al_2O_3$ catalyst for methanol synthesis from CO_2: Insights from experiments and DFT-based microkinetic modeling, *Appl. Catal., B*, 2023, **332**, 122743, DOI: **10.1016/j.apcatb.2023.122743**.